Time-varying stimuli that prolong IKK activation promote nuclear remodeling and mechanistic switching of NF-κB dynamics

Authors

Steven W. Smeal[1], Chaitanya S. Mokashi[1,2], A. Hyun Kim[1], P. Murdo Chiknas[1], Robin E. C. Lee[1,3,†]

Affiliations

[1]Department of Computational and Systems Biology, School of Medicine, University of Pittsburgh, Pittsburgh, PA 15213, USA

[2]current address Altos Labs, Redwood City, CA, 94065, USA

[3]Center for Systems Immunology, School of Medicine, University of Pittsburgh, Pittsburgh, PA 15213, USA

Other footnotes

[†]Corresponding Author: robinlee@pitt.edu

Abstract

Temporal properties of molecules within signaling networks, such as sub-cellular changes in protein abundance, encode information that mediate cellular responses to stimuli. How dynamic signals relay and process information is a critical gap in understanding cellular behaviors. In this work, we investigate transmission of information about changing extracellular cytokine concentrations from receptor-level supramolecular assemblies of IκB kinases (IKK) downstream to the nuclear factor κB (NF-κB) transcription factor (TF). In a custom robot-controlled microfluidic cell culture, we simultaneously measure input-output (I/O) encoding of IKK-NF-κB in dual fluorescent-reporter cells. When compared with single cytokine pulses, dose-conserving pulse trains prolong IKK assemblies and lead to disproportionately enhanced retention of nuclear NF-κB. Using particle swarm optimization, we demonstrate that a mechanistic model does not recapitulate this emergent property. By contrast, invoking mechanisms for NF-κB-dependent chromatin remodeling to the model recapitulates experiments, showing how temporal dosing that prolongs IKK assemblies facilitates switching to permissive chromatin that sequesters nuclear NF-κB. Remarkably, using simulations to resolve single-cell receptor data accurately predicts same-cell NF-κB time courses for more than 80% of our single cell trajectories. Our data and simulations therefore suggest that cell-to-cell heterogeneity in cytokine responses are predominantly due to mechanisms at the level receptor-associated protein complexes.

Introduction

The typical body of an adult human has 10s of trillions of cells[1], and in some cases, individual cell behaviors can affect the entire organism. When cells are exposed to different biologic cues in their microenvironment, such as inflammatory cytokines, they activate dynamic signal transduction networks that mediate vital cell fate decisions. Deregulation of these networks contributes to a panoply of autoimmune diseases and cancers[2-4]. Variability and nonlinearity are typical characteristics of cellular signal transduction that limit our understanding of healthy and diseased cell behaviors and decisions processes. Variability arises from intrinsic and extrinsic sources of biochemical noise associated with stochastic molecular interactions that impact transcription rates, protein expression, among other biological processes[5-8]. Meanwhile, nonlinearity emerges due to complex biomolecular networks that include a host of feedback and feedforward loops. Adding to this complexity, the extracellular environment is dynamic, and cells are constantly exposed to multiple signaling molecules with changing concentrations. The combined effects of variability, nonlinearity, and dynamic input signals contribute to versatility of signaling pathways to regulate a wide range of responses. Therefore, experiments that combine single cell dynamics with computational modeling are important to reveal the capabilities of signaling systems and understand their emergent properties[9].

When inflammatory cytokines in the extracellular milieu activate transmembrane cytokine receptors, clustered receptors recruit cytoplasmic adaptors and enzymes to form a supramolecular protein assembly near the plasma membrane[10,11]. As the assembly matures, polyubiquitin scaffolds form around the protein core. A hallmark of cytokine

72 responses is recruitment-based activation of IKK kinase complexes to assemblies through
73 the ubiquitin binding domain of NEMO, the IKK regulatory subunit[12-15]. Using fluorescent
74 protein (FP) fusions of NEMO, individual assemblies can be visualized by live-cell
75 microscopy as diffraction-limited puncta near the plasma membrane[16,17]. The mature
76 protein assembly is a signal integration hub that activates IKK to coordinate downstream
77 inflammation-driven NF-κB signaling. Although the supramolecular assemblies, referred to
78 as 'complex I' (CI)[10,11], were first characterized for responses to tumor necrosis factor (TNF),
79 interleukin-1ß (IL-1) and other cytokines produce CI-like assemblies with cytokine-specific
80 receptors and adaptor proteins. CI and CI-like assemblies are reliant on different
81 combinations of ubiquitin chain scaffolds[15,16]. However, all regulate IKK activation via
82 induced proximity of IKK with other signaling mediators that reside on the assembly[18]. For
83 simplicity, we refer to the family of CI and CI-like assemblies simply as 'CI'.

84 IKK activity following induction of CI promotes degradation of NF-κB inhibitor proteins
85 (IκB) in the cytoplasm, and nuclear accumulation of NF-κB transcription factors[19]. Temporal
86 properties of NF-κB in the nucleus encodes a dynamic transcriptional signal, regulating
87 diverse gene expression programs that promote cell survival and propagate inflammatory
88 signals. Live-cell tracking of FP fusions of the RelA subunit of NF-κB have provided
89 instrumental data to understand and model transcriptional mechanisms and emergent
90 properties that place the NF-κB pathway among exemplars of dynamical biological
91 systems[20-22]. Key to these discoveries are negative feedback mediators, particularly IκBα,
92 that are transcriptionally regulated by NF-κB. Following NF-κB activation, newly synthesized
93 IκBα promotes nuclear export and cytoplasmic sequestration of NF-κB, restoring its baseline

94 cytoplasmic localization. Combined experiments and models have revealed mechanisms
95 for dynamical regulation of nuclear NF-κB and transcriptional feedback; however, we have
96 limited understanding of how information from dynamic extracellular signals is encoded and
97 decoded within cells by the IKK-NF-κB signaling axis.

98 Typically, cellular signaling pathways have been studied using dose-response
99 approaches that expose cells to continuous and unchanging extracellular stimuli. While
100 responses to static concentrations provide a foundational readout for investigating cell
101 behaviors, they are neither comparable to the dynamic signals observed *in vivo* nor sufficient
102 to fully probe the versatility of cellular responses. We and others have recently shown that
103 dynamic cell cultures can be achieved using PDMS- or acrylic-based microfluidic flow
104 devices that vary with trade-offs between complexity, precision, and multiplex capabilities[23-
105 26]. In most cases, single cell studies of signal transduction in dynamic microenvironments
106 have revealed unexpected emergent properties that have inspired significant refinement of
107 models that aim to predict and understand the underlying biological circuits[27-31].

108 In this work, we investigate IL-1 induced signaling in U2OS osteosarcoma cells to
109 understand how information for time-varying extracellular cytokines is encoded within cells.
110 The dual reporter cells were CRISPR-modified for endogenous FP fusions to observe active
111 receptor complexes through supramolecular assemblies of EGFP-NEMO, the regulatory IKK
112 subunit, and downstream dynamics of an mCherry-fusion of the NF-κB RelA subunit. Using
113 live-cell imaging in a custom robot-controlled microfluidic cell culture system, we
114 simultaneously measure upstream and downstream reporters in single cells exposed to
115 dynamic stimuli. By observing I/O encoding of IKK-NF-κB signals and comparing cells

116 exposed to a single cytokine pulse with varied duration, we show monotonicity between the
117 aggregate of activated receptor complexes and downstream TF dynamics. This result is
118 consistent with our previous investigation of cells exposed continuously to static cytokine
119 concentrations[17]. Remarkably, monotonicity of I/O encoding breaks down when cells are
120 exposed to a series of short cytokine pulses. We observe that dynamic TF responses to pulse
121 trains are significantly greater than expected from a single pulse, even when pulse trains are
122 compared to a bolus of a larger overall cytokine dose. Enhanced TF responses to a cytokine
123 pulse train can be attributed to marked alteration of nuclear export dynamics of NF-κB,
124 transitioning from first-order to sustained zero-order kinetics in cells where activated
125 receptor complexes persists for longer than 80 minutes. Using particle swarm optimization,
126 we demonstrate that a mechanistic model does not recapitulate this emergent property of
127 the IKK-NF-κB signaling axis and fails to switch to zero-order kinetics in response to a pulse
128 train. By contrast, adding mechanisms for DNA binding and NF-κB-dependent chromatin
129 remodeling, the resulting models recapitulate all the experimental findings. Our model
130 suggests that temporal dosing that prolongs IKK activation facilitates pseudo-zero-order
131 switching by two coupled mechanisms that prolong nuclear NF-κB retention without
132 requiring persistent or saturating conditions: i) by promoting permissive chromatin states
133 that expose new NF-κB binding sites; and consequently ii), by limiting the concentration of
134 free nuclear NF-κB available to regulate expression of negative feedback mediators.
135 Furthermore, simulations using the calibrated model to resolve experimental CI time
136 courses from a complete set of single-cell validation data that were not used during
137 optimization, accurately predicts same cell NF-κB responses for over 80% of single cell time

138 courses. Together, our results demonstrate that when overall cytokine dosage is limited,
139 temporal stimuli can encode distinct cellular behaviors, and that cell-to-cell variability in
140 cytokine responses is largely accounted for by variability of receptor-level mechanisms.

141 **Results**

142 **IL-1 pulse duration produces a monotonic correlation between same-cell IKK and NF-**

143 **κB responses**

144 We previously developed a CRISPR-modified U2OS cell line that co-express FP fusions of
145 NEMO (EGFP-NEMO) and RelA (mCh-RelA) from their endogenous loci. These dual-reporter
146 cells were used to investigate the IKK-NF-kB signaling axis in cells exposed to continuous
147 stimuli[17]. By simultaneously measuring time courses of fluorescence intensity for
148 supramolecular assemblies of EGFP-NEMO as a reporter for CI and nuclear NF-kB in the
149 same cell, these studies revealed fundamental aspects of signal encoding in the pathway.
150 We reported that extracellular cytokine concentrations control the numbers and timing of
151 formation for CI assemblies. Experiments that tracked EGFP-NEMO at individual CI
152 assemblies revealed that fluorescence intensity time-courses of single puncta are invariant
153 between different cytokine concentrations. Further experiments revealed cytokine-specific
154 encoding, where a quantized number of EGFP-NEMO molecules is recruited at each CI
155 structure. Here, TNF-induced receptor assemblies are shorter-lived and recruit
156 approximately 30% the peak amount of EGFP-NEMO when compared with brighter and
157 longer-lived IL-1-induced assemblies. Finally, we observed that activity from CI puncta is
158 pooled for downstream signal transmission where the aggregate area under the curve (AUC)
159 of CI puncta numbers is a strong same-cell predictor of the AUC nuclear NF-kB response.

160 Our previous results helped define the rules of signal encoding in terms of cytokine-
161 specificity and static cytokine concentrations. However, these experiments did not
162 investigate the orthogonal axis of how time-varying patterns of cytokines influence IKK-NF-

163 κB signaling. We therefore set out to probe the pathway by first measuring the dynamics of
164 IKK and NF-κB responses as a function of cytokine pulse duration. To generate cytokine
165 pulses while simultaneously performing high magnification single-complex imaging, we
166 leveraged a recently developed dynamic stimulation system (DSS). The DSS consists of a
167 custom robotic gravity pump controller that coordinates laminar fluid streams in a paired
168 microfluidic cell culture device[24]. The microfluidic device was simplified from the previous
169 DSS instrumentation as a two-inlet cell culture chamber (Fig. 1a, Supplementary Fig. 1, and
170 Supplementary File 1). Here, one inlet is attached to a fluid reservoir with a mixture of
171 cytokine, indicator dye, and cell culture medium, and to the other, a reservoir with medium
172 only. Using the gravity pump to vertically relocate the fluid reservoirs generates hydrostatic
173 pressure differentials at the inlets of the microfluidic device and positions the laminar
174 cytokine-containing stream over the cells within (Fig. 1b). By varying the relative heights of
175 the cytokine-containing and medium-only reservoirs, the system can be used to generate
176 pulses in the experimental region of the cell culture device (orange boxes, Fig. 1b). In
177 principle, the automated system described here operates like a manually controlled system
178 we described previously[23], but with enhanced precision, reproducibility, and constant flow
179 rates[24].

180 Using our dual-reporter cell line, we investigated the same-cell dynamics of NEMO
181 assemblies and NF-κB nuclear translocation in a microfluidic device. We focused on cellular
182 responses to 10ng/mL of IL-1, a non-saturating cytokine concentration that produces vibrant
183 NEMO assemblies and unambiguous nuclear NF-κB responses[17]. Consistent with our
184 previous results, dual-reporter cells in the device showed transient localization of EGFP-

185 NEMO to CI-like complexes, peaking in numbers by approximately 20 minutes, and robust
186 nuclear translocation of mCh-RelA (Fig. 1c, and Supplementary Movie 1). Next, we
187 measured single cell time-courses of EGFP-NEMO puncta and nuclear mCh-RelA in
188 response to a single IL-1 pulse across a range of durations. Previously, we showed that time-
189 integrated AUCs for trajectories of NEMO spot numbers and nuclear RelA fold change are
190 scalar descriptors of single cell time courses that encode the most information about
191 cytokine concentration[32,33]. Consistent with these results, AUCs of EGFP-NEMO spot
192 numbers and nuclear mCh-RelA in single cells show increasing responsiveness with pulse
193 duration and form a strongly monotonic continuum of same-cell correlations (Fig. 1d-f).
194 Previous works have shown that mammalian cell lines may follow an 'area-rule',
195 where the fraction of responsive cells and overall NF-kB activation strength is proportional
196 to the product of concentration and duration of cytokine stimulation[23,34]. Our current results
197 are consistent with the 'area-rule', showing that information about extracellular pulse
198 duration is also well determined when observed upstream via EGFP-NEMO puncta that
199 provide an estimate for CI activation. Next, we asked if the area rule remains true for
200 increasingly complex patterns of dynamic cytokine stimulation.
201
202 **Cytokine pulse trains produce significantly greater NF-kB responses than expected**
203 **from a single pulse**
204 Cytokines typically have short half-lives *in vivo*, particularly for TNF and IL-1 that are rapidly
205 cleared from the bloodstream within minutes[35-37]. Since inflammatory secretions in the
206 vicinity of activated immune cells are also likely to be concentration and duration limited,

207 with localized depletion effects[38], cells may experience cytokines as a more rapid series of
208 short pulses. Pulses of inflammatory cytokines have been shown to selectively regulate long
209 lasting transcriptional programs. For example, in neuroblastoma cells, a single 5-minute
210 pulse of TNF can initiate transcription of NF-kB-regulated early response genes that persist
211 for hours, but not late response genes that require either constant or repeat cytokine
212 stimulation[21]. We therefore asked whether a succession of short cytokine pulses in the
213 extracellular milieu is encoded distinctly by the IKK-NF-kB axis, or if responses to a pulse
214 train follows an 'area rule' equivalent to a single bolus of same overall dose.

215 We compared cellular responses between a single 6-minute pulse that produces an
216 intermediate response strength (Fig. 1c and d), and multiple shorter pulses with the same
217 cumulative IL-1 exposure but spread out in time. We partitioned a single 6-minute pulse
218 equally into either two, three or four short pulses, and compared inter-pulse gap durations
219 between 5 and 20 minutes (Fig. 2 and Supplementary Fig. 2). In comparison with a single 6-
220 minute pulse, time-courses for NEMO puncta numbers in response to pulse trains showed
221 lower peak values and longer spot persistence (Fig. 2a). Although in some pulse train
222 conditions there was a subtle overall increase in AUC of NEMO puncta, these values typically
223 did not reach significance and remained smaller than exposure to a larger single 15-minute
224 pulse (Fig. 2 and Supplementary Fig. 2). Remarkably, despite only subtle and often non-
225 significant increases in the AUC of IKK responses, many of the pulse-train conditions
226 showed significant increases in the AUC of nuclear mCh-RelA time-courses (Fig. 2B). Even
227 though pulse trains produced comparable peak amounts of nuclear RelA with similar timing
228 to a dose-conserving single bolus, contributing to the stronger NF-kB AUC response was

229 markedly slower nuclear export. Nuclear export of NF-kB following a pulse train appeared
230 almost linear, following zero-order kinetics. Nuclear export of RelA in response to a pulse
231 train contrasts with most single pulse responses less than 30 minutes, which exhibit
232 exponential nuclear export, as expected from first- and higher-order biomolecular reactions
233 (Fig. 2 and Supplementary Movie 2). The enhancement effect of linear nuclear RelA export
234 is exemplified by the condition with four 1.5-minute pulses of IL-1 separated by a 5-minute
235 gap (4x1.5), which showed a greater than 2-fold increase in overall AUC. The nuclear RelA
236 response strength for the 4x1.5 condition even surpassed responses to a 15-minute pulse
237 despite the former having less than half the total cytokine exposure (Fig. 2B and
238 Supplementary Movie 3). Finally, monotonicity of same-cell correlations between AUCs of
239 NEMO spots and nuclear RelA was disrupted for pulse train conditions (Fig. 2C).

240 The unexpected increase in the response strength of nuclear RelA to a pulse train is
241 an emergent property of the signaling pathway. We next asked whether the emergent
242 property is specific to cytokine or cell type and found that strongly TNF-responsive KYM-1
243 rhabdomyosarcoma cells that express FP-RelA[23,33] show similarly enhanced responses to
244 TNF pulse trains (Supplementary Fig. 3). Notably, some pulse train conditions diminish the
245 emergent property effect. For example, conditions with fewer pulse numbers and longer
246 inter-pulse gap lengths in the order of 10-20 minutes tend to have weaker nuclear RelA
247 responses for both cell types and both cytokines (Supplementary Figs. 2 and 3). Together,
248 these results suggest that cells can bypass the area rule in response to dynamic milieus and
249 encode more information through CI assemblies than is represented by the scalar AUC of
250 NEMO puncta.

251

252 **Stimulation patterns that prolong NEMO puncta shifts the mechanism of NF-kB nuclear**

253 **export**

254 Since the AUC of NEMO puncta could not explain enhanced nuclear NF-kB in response to a

255 pulse train, we asked if other quantitative features of EGFP-NEMO single cell time courses

256 reflect the emergent property. When temporal features were quantified from NEMO time

257 courses, distributions for both the timing of maximal (t_{max}) and time to adaptation (t_{adapt}) of

258 NEMO spot numbers showed trends like the AUC of nuclear RelA (Fig. 3a-c).

259 Next, we set out to establish quantitative features of EGFP-NEMO that correlate with

260 features of nuclear RelA. Because the maximum of nuclear RelA fold change did not show a

261 strong trend between pulse-trains and dose-conserving single-pulses, we focused on

262 scoring rates of nuclear RelA export (Fig. 3d and Supplementary Fig. 4a). As mentioned

263 earlier, we visually observed that dynamics for nuclear RelA export appeared to switch from

264 a first order to a pseudo-zero-order reaction (Figs. 2a and 3d) in response to a pulse train. To

265 quantify this observation, single-cell nuclear RelA export dynamics were fitted to two

266 models that represent zero-order and first-order kinetics (Supplementary Fig. 4b; and see

267 methods). In the results, increasingly positive scores indicate a progressively stronger zero-

268 order exit rate, while negative values correspond to first-order exit rates. We observed that

269 single 6-minute and 15-minute pulse shows strong first-order dynamics and the responses

270 to pulse trains showed strong zero-order kinetics (Supplementary Figs. 1c, d and 4c). Finally,

271 we correlated features of EGFP-NEMO against the nuclear RelA export order score. Although

272 t_{max} of NEMO only correlated weakly, by contrast, t_{adapt} of NEMO showed a strong monotonic

273 correlation with the nuclear RelA exit rate score (Fig. 3e, f). Based on our data, stimulation
274 profiles that prolong CI assemblies beyond 80 minutes shift the nuclear export rate of RelA
275 towards a pseudo-zero-order process and thus enhance the AUC of the nuclear NF-kB
276 response.
277
278 **A model with chromatin remodeling recapitulates the emergent property and nuclear**
279 **NF-kB export**
280 Mechanistic models provide mathematical representations of biological systems, enabling
281 researchers to test hypotheses and synthesize their understanding of system-level
282 behaviors. Ordinary differential equation-based models of the NF-kB transcriptional system
283 have been deeply informative. Previous models parameterized to quantitative assays and
284 single cell data have been used to investigate nuclear translocation dynamics of NF-κB,
285 emphasizing negative feedbacks from IκB isoforms[39] and A20[21], as well as mechanisms for
286 fold change detection (called D2FC, derived from previous models)[32]. Each of these models
287 has been built upon their predecessors to answer different questions. However, none of the
288 models have been parameterized to single receptor-complex data and dynamic stimuli.
289 To explore the possible biological mechanisms that contribute to zero-order
290 switching and enhanced nuclear RelA retention in response to a pulse train, we first asked if
291 the D2FC model directly recapitulates experiments. Since we have a compendium of single
292 cell data from dual-reporter cell lines, we modified the model to activate IKK directly from
293 experimental time courses of EGFP-NEMO puncta and simulate nuclear NF-κB responses
294 (Fig. 4a). We first tested the previously published parameterization of the D2FC model, using

295 a fitted scaling parameter to interface experimental data for EGFP-NEMO puncta that
296 produces a best fit simulated NF-κB response (see methods). Although the naive D2FC
297 model replicates the AUC of NF-κB for responses to a single pulse, the model results did not
298 show increased AUC of nuclear NF-κB nor switching to zero-order export mechanisms when
299 simulations were run using EGFP-NEMO pulse-train data as inputs (Supplementary Fig. 5).

300 Next, we tested if the topology of the D2FC model can reproduce the emergent
301 property using parameter optimization. Particle swarm optimization (PSO) is a bio-inspired
302 algorithm that searches parameter space for candidate solutions, using an objective
303 function to measure the quality of fit for each[40]. Implementations of PSO often identify nearly
304 global optimal parameterizations in high-dimensional and rugged objective landscapes. To
305 decrease the computational time, we considered a minimal dataset of 4 experimental
306 conditions that manifest the emergent property (consisting of control, 1x6min, 4x1.5min,
307 and 1x30min pulse data; Fig. 4a top panel). Subsequently, we used PSO to simulate
308 responses to the average of EGFP-NEMO time-courses from each condition, using the
309 average of nuclear mCh-RelA for each condition as the objective function (Fig. 4A). PSO was
310 repeated 500 times to generate parameter sets that sample the model's best fits to data. For
311 the 500 parameter sets, we performed post-hoc analysis to evaluate three error criteria for
312 each: i) error in producing a nearly 2-fold increase in the AUC of nuclear NF-κB comparing
313 1x6min and 4x1.5min conditions, referred to as the 'emergent property' score; ii) the average
314 sum squared error (<SSE>) of fits to the 4 training conditions; and, (iii) the SSE of fits to
315 validation data consisting of 5 mean experimental conditions that were not used for PSO
316 (Fig. 4b). Remarkably, each of the optimized D2FC models had high error scores across

317 evaluation criteria (Fig. 4b), failing to recapitulate the system's emergent property
318 (Supplementary Fig. 5c). Taken together, the results suggest that the topology of the D2FC is
319 missing critical circuitry that is necessary to explain the experimental observations.

320 Pseudo-zero-order processes are unusual behaviors in biological systems because
321 they appear to be independent of reactant concentrations. Typically, zero-order kinetics
322 result from systems where one of the reactants is greatly limited or scaffolded into a lower
323 reactivity state. Since NF-κB is well established as a transcription factor, we hypothesized
324 that NF-κB binding to broadly to DNA[41-45] may be an essential mechanism that is not explicit
325 in the D2FC model. Furthermore, there is a growing body of literature that characterizes
326 chromatin remodeling capabilities of NF-kB. For example, NF-kB can bind to assembled
327 nucleosomes and flanking DNA, contributing to DNA unwrapping and nucleosome
328 displacement[46,47]. Chromatin reorganization was found to decode the duration of nuclear
329 NF-kB, where prolonged nuclear TF contributes to stimulus- and gene-specific transcription
330 initiation by progressively revealing promoter sequences that are otherwise closed in basal
331 conditions[48]. More recently, prolonged non-oscillatory nuclear NF-kB was shown to cause
332 cytokine-inducible alterations to chromatin accessibility near NF-kB binding sequences,
333 activation of latent enhancers, and epigenetic reprogramming[22]. Therefore, additional
334 mechanisms were added to the model, to include NF-kB binding to DNA and chromatin
335 remodeling that reveals additional NF-kB binding sites via mechanisms akin to pioneering[49]
336 (see methods). The modified D2FC model with chromatin remodeling is referred to as D2FC-
337 squared ($D2FC^2$) henceforth (see methods, Supplementary Tables 1 and 2).

338 Using PSO, we again sampled 500 parameter sets with the $D2FC^2$ architecture. The

339 D2FC^2 model produced high quality fits, significantly reducing scores of the 3 error criteria
340 (Fig. 4B). Parameterization sets of the D2FC^2 from PSO showed that the approach effectively
341 explored the prior distribution of acceptable parameters, and the top 10 scoring models
342 were able to achieve a similar quality of results despite being derived from distinct
343 combinations of parameters (Fig. 4B, and Supplementary Fig. 6). Taken together, the
344 topology of D2FC^2 enables the model to recapitulate the average behaviors of all
345 experimental conditions, with robustness to variation of parameters.
346

347 **A model with chromatin reorganization accurately predicts single cell responses and**
348 **experiments**

349 Training and validation simulations with the D2FC^2 model used averages of experimental
350 single cell time courses for each condition, both as inputs to simulations and to evaluate the
351 quality of fits. We next asked whether the D2FC^2 accurately predicts single-cell dynamics.
352 Using the 3 error criteria to rank the models, the top-performing parameter set in the D2FC^2
353 was selected for further analysis (Fig. 4b, red asterisk). Single-cell EGFP-NEMO time-
354 courses from all the single pulse and pulse train conditions were as inputs to simulate
355 nuclear NF-kB responses. Visually, simulated single-cell time courses of nuclear NF-kB
356 appeared like experiments, showing both first-order and zero-order nuclear export kinetics
357 appropriate to each condition (Fig. 5a). AUCs of simulated nuclear NF-kB to single pulse
358 conditions showed dose-responsiveness, and consistent with expectations based on error
359 scores following PSO, D2FC^2 simulations for pulse trains recapitulated the emergent
360 property (Fig. 5b and c). Furthermore, interquartile ranges of boxplots were similar when

361 comparing experiments and simulations, suggesting that cell-to-cell variability at the level
362 of CI dynamics contributes significantly to variability of nuclear NF-kB dynamics observed
363 in single-cell experiments.

364 Following, we moved away from population average data and evaluated the quality
365 for single cell fits by measuring the SSE between experimental nuclear RelA trajectories and
366 simulated NF-kB dynamics. An elbow plot was used to define the error threshold to classify
367 low- and high-quality fits, and a stricter threshold was applied to define a third class of
368 'excellent fits' where experiment and simulations overlap almost perfectly (Supplementary
369 Fig. 7). When compared between experimental conditions, performance of the $D2FC^2$ was
370 consistent with most single cells showing high- and excellent-quality fits (Fig. 5d, left). The
371 single 15-minute pulse and the 3x2min were the conditions that showed the most low-
372 quality fits; nevertheless, even these weakest conditions still achieved excellent or high-
373 quality fits for approximately 70% of single cell trajectories. Comparing the top 10 $D2FC^2$
374 parameter sets, all recapitulate single pulse dose-responsiveness and the emergent
375 property, as well as produce high-to-excellent predictions for over 80% of the single cell
376 nuclear RelA trajectories aggregated across all conditions (Fig. 5d, right; see also
377 Supplementary Table 3). These results demonstrate that many different parameterizations
378 of the $D2FC^2$ architecture can robustly resolve single-cell EGFP-NEMO time courses and
379 predict nuclear RelA responses across a heterogeneous population of cells.

380 Finally, we asked whether the $D2FC^2$ can predict the impact on nuclear RelA
381 dynamics in the presence of a chromatin perturbation. Azacitidine is cytidine analog that
382 incorporates into DNA and inhibits DNA-methyltransferase DNMT1, promoting

383 hypomethylation and chromatin relaxation over timescales of days[50]. To model the effects of
384 azacytidine, the term representing basal DNA accessibility was increased and the model
385 was allowed to adapt to a new steady state before resolving the average EGFP-NEMO time
386 course for a 6-minute pulse. The simulations revealed two trends: first, that progressively
387 relaxed chromatin leads to increased basal abundance nuclear RelA; second, that fold-
388 change responses of nuclear RelA following cytokine stimulation are effectively reduced
389 (Fig. 6a and b). To test these model predictions, cells were cultured in the presence of
390 azacytidine for 3 or 6 days before exposure to a single 6-minute pulse of IL-1. Although 3 days
391 of culture with azacytidine appeared like untreated control cells, 6-day samples were
392 consistent with the model, showing significant enrichment of basal RelA prior to stimulation
393 and suppressed nuclear RelA dynamics in response to IL-1 (Fig. 6c, d, and Supplementary
394 Fig. 8). Thus, chromatin organization influences cytokine-induced temporal profiles of
395 nuclear NF-kB.
396
397 **Peak number and adaptation time of CI fine tunes chromatin permissiveness and**
398 **nuclear NF-kB dynamics**
399 Temporal profiles of IKK activity encode information about the abundance and type of
400 inflammatory factors in the milieu, regulating nuclear NF-kB and stimulus-specific gene
401 expression programs[17,51]. Our results here show that features of IKK at CI assemblies also
402 encode information about temporal presentation of cytokines, such as their numbers and
403 timing, that in succession regulate feedback pathways in the nucleus (Fig. 7a).
404 Based on single cell time courses of EGFP-NEMO from static cytokine

405 concentrations[17], single cytokine pulses (Fig. 1), and cytokine pulse trains (Fig. 2), CI-
406 encoding can be decomposed into a primary peak and a second slow-adapting distribution
407 (Fig. 7b). We leveraged the D2FC[2] to systematically evaluate the impact of CI-encoding
408 features on downstream signaling (Fig. 7c). First, we considered nuclear NF-kB fold change,
409 which we showed previously to correlate strongly with NF-kB-regulated early response
410 genes[32]. Here, maximal nuclear NF-kB correlates with peak CI numbers that saturate around
411 300, and adaptation time for the secondary distribution had negligible impact (Fig. 7c, top
412 left). Comparing rates of nuclear NF-kB export showed a non-linear relationship with CI-
413 encoding features. A primary peak of approximately 50 CI puncta and adaptation times of
414 greater than 80 minutes were both strictly required for conversion of nuclear NF-kB export
415 rates from a first order to pseudo-zero-order process (Fig. 7c, top right). Higher peak CI
416 numbers required even longer adaptation times to achieve zero-order NF-kB export kinetics,
417 possibly requiring greater CI persistence to compensate for stronger first-wave transcription
418 negative feedback mediators, such as IkBα. Chromatin openness showed a similar pattern,
419 requiring a minimum peak CI of nearly 100 puncta, and prolonged activation to increase
420 overall permissiveness (Fig. 7c, bottom left). Even the highest peak CI numbers failed to
421 enhance chromatin opening unless adaptation time also persisted for more than 60-80
422 minutes. Finally, since open chromatin reveals new NF-kB binding sites, both productive and
423 non-productive in regulating gene transcription, we measured the fraction of free nuclear
424 NF-kB as a function of chromatin status. Remarkably, even when concentrations of nuclear
425 NF-kB are at their highest, permissive chromatin can deplete free nuclear NF-kB (Fig. 7c,
426 bottom right). Therefore, despite high total concentrations of nuclear NF-kB, permissive

427 chromatin at later times may only leave trace amounts of free nuclear TF to interact with
428 promoters of early response genes such as IkBα.

429 Studying I/O relationships in dual-reporter cells exposed to dynamic stimuli, while
430 leveraging naturally occurring cell-to-cell variability, revealed features of CI encoding that
431 regulate time profiles of nuclear NF-kB. Simulations with the D2FC[2] show that the primary
432 peak of CI determines the fold change of nuclear NF-kB and the adaptation time facilitates
433 switching towards more permissive chromatin states with additional NF-kB binding sites.
434 Importantly, DNA-based sequestration of nuclear NF-kB is transient, and the model allows
435 nascent IkBα polypeptides to interact with DNA-bound NF-kB to facilitate dissociation, as
436 seen in experiments[52]. Together, our experiments and simulations suggest that the transition
437 to a pseudo-zero-order export process results from the combined effect of sequestration
438 and feedback depletion on early gene promoters.

439 **Discussion:**

440 On the surface of a human cell, the number of IL-1 and TNF receptors is relatively small,
441 estimated in the range of hundreds to low thousands per cell[17,53]. Following cytokine
442 stimulation, ligated receptors are rapidly internalized and degraded [54,55]. Therefore, a limited
443 and depletable resource of surface receptors is available to encode information about the
444 inflammatory milieu into the cell via CI assemblies. We reasoned that cytokine conditions
445 that spread out a stimulus in time may encode different signals from tonic and saturating
446 boluses that would rapidly deplete the available receptor pool. To this end, our result shows
447 that temporal properties of IKK encode information about time-varying extracellular
448 conditions that can be used by the cell in succession to regulate distinct temporal response
449 patterns of nuclear NF-κB.

450 We used dynamic stimuli, dual-reporter cells, and computational models to
451 investigate information encoding properties of the IKK-NF-κB signaling axis. Exposing dual-
452 reporter cells to a single cytokine pulse revealed that the aggregate AUCs of IKK and nuclear
453 NF-κB increase with the IL-1 pulse duration, forming a continuum of single cell I/O responses
454 (Fig. 1f). In contrast, when a cytokine is presented as a series of short pulses, monotonicity
455 of the aggregate I/O response is disrupted with cells showing disproportionately enhanced
456 AUCs for nuclear NF-κB responses (Figs. 2 and 3). We determined that the aggregate AUC of
457 IKK puncta is not sufficient to predict same-cell NF-κB responses to dynamically presented
458 stimuli. Instead, orthogonal axes for peak numbers and adaptation times of CI were
459 predicted to encode signals that enhance NF-κB responses by mechanisms that switch
460 nuclear export from a first- to pseudo-zero-order process. Although both features are

important contributors, CI adaptation times where EGFP-NEMO puncta persist for around 80 minutes or longer define a threshold for conversion to zero-order kinetics. This observation is reminiscent of a previous computational prediction where a constant plateau of low-amplitude IKK activity following can mediate long-lasting nuclear NF-κB time profiles[51]. Nevertheless, experiments differ from these predictions because CI assemblies and IKK kinase assays in wild-type cells[16,17,51,56] show adaptation, typically within 60-90 minutes following exposure to TNF or IL-1. Based on our experiments and model results, we surmise that the tail of IKK activity that extends beyond 80 minutes is crucial to blunt the first wave of IκBα-mediated feedback, subsequently facilitating nuclear remodeling that supports zero-order export kinetics.

In contrast with experiments, and regardless of model parameterization, simulations with the D2FC model[32] to predict NF-κB responses did not show switching between first- and zero-order nuclear export kinetics, and the emergent property with enhanced response AUCs. The D2FC[2] modified the base model by invoking explicit DNA-binding and chromatin-remodeling mechanisms for NF-κB. These were selected because they reflect increasingly well-characterized mechanisms that can create reactant-limiting conditions necessary for a pseudo-zero-order process. To illustrate this point, NF-κB binds to hundreds of non-redundant sequences that are distributed with repetition throughout the human genome[43,57]. Early estimates predicted that there are significantly more binding sites in the genome than the ~10^5 NF-κB molecules in a typical mammalian cell[41]. Subsequently, tens of thousands of NF-κB binding sites have been observed in macrophages and B cells, as well as enrichment of NF-κB binding on the 5' end of genes or other non-promoter sequences[42,44,45]. More recent

483 results using genetic knockout of IkBα in mouse BMDMs showed prolonged nuclear NF-κB
484 following TNF stimulation, along with disruption of nucleosomal histone-DNA interactions
485 in the vicinity of NF-κB binding sites[22]. Since earlier studies did not use genetic or chemical
486 perturbations that are necessary to produce prolonged nuclear NF-κB responses and
487 chromatin reorganization in differentiated immune cells, they are likely to underestimate the
488 breadth of NF-κB-DNA interactions. Taken together, there is a vast abundance of productive
489 and non-productive NF-κB-DNA interactions that are basally accessible, and significantly
490 more following chromatin reprogramming[48]. Incorporation of these roles in the D2FC^2
491 revealed that consequences of DNA-binding and chromatin are sufficient to switch nuclear
492 NF-κB export to a pseudo-zero-order process. Consequently, our results also suggest that
493 mechanisms associated with chromatin dynamics and epigenetic reprogramming are
494 selected via dynamic stimuli that control the timing and numbers of CI. There is growing
495 recognition of multi-hit immune signaling where cytotoxicity is additive over multiple sub-
496 lethal interactions between immune and cancer cells[58,59]. With these observations, our
497 results support that dynamic cytokine presentations, such as multi-hit pulses, may encode
498 distinct messages to receiving subpopulations of non-immune cells, including cancers.

499 By using PSO to fit averaged experimental data from four conditions that embody the
500 emergent property, families of model parameterizations were identified that successfully
501 recapitulate experiments. As discussed earlier, the D2FC^2 model architecture was modified
502 for chromatin permissiveness and DNA binding only, and did not invoke any additional
503 molecular species or mechanisms. Simulations *in silico* further demonstrated capabilities
504 of D2FC^2 to accurately predict single cell NF-κB responses from time courses of CI, validated

505 with a compendium of experimental trajectories from dual reporter cells. Given that there
506 were no single-cell data used during optimization, it was remarkable that a family of different
507 model parameterizations was found, each capable of accurately predicting same-cell NF-
508 κB responses from experimental EGFP-NEMO time profiles. The added mechanisms of
509 D2FC[2] are robust, allowing the resulting system to achieve consistent behavior without
510 requiring strict expression levels for all molecular species in the model that individually tend
511 to exhibit variability when measured in single cells. Taken together, low numbers for cytokine
512 receptors and stochasticity of their interactions are among the chief contributors to
513 heterogeneity between single cell NF-κB responses, which can be accurately predicted from
514 CI-level measurements.

515 Dynamics of nuclear NF-κB mount stimulus-specific adaptive responses through
516 selective regulation of gene expression programs, many of which cluster into early-, mid-,
517 and late-response categories[21,51,60]. Although late response genes are typically associated
518 with tonic and high-concentration inflammatory stimuli, this may not be strictly required.
519 Based on our experiments and model, we speculate that mid- and late-response genes can
520 arise from chromatin accessibility, and that certain temporal stimuli that distribute CI
521 numbers in time have the potential to reveal their promoters via chromatin remodeling.
522 However, follow-up studies to test this possibility will require further refinements to our
523 model. For example, the mechanism for chromatin remodeling in the D2FC[2] is likely to be an
524 oversimplification, lacking mechanisms for gene-specific promoter accessibility and other
525 DNA-binding proteins such as AP-1 that remodel chromatin in response to inflammation[61,62].
526 Similarly, theoretical IKK distributions studied in the model may be difficult to achieve

experimentally, and another layer of detail is necessary to accurately predict the distribution of peak numbers and timing from complex environmental stimuli. Nevertheless, we expect that forthcoming models will explicitly model CI puncta and gene-specific promoters relative to chromatin. Through a comprehensive model, we will understand how basal conditions of different cell types encode and decode certain cytokine responses, and how complex environments can select gene expression programs using CI and IKK as signaling hubs.

In summary, our results demonstrate that the number and timing of CI assemblies encode information about time-varying stimuli in the extracellular milieu. With limited numbers of surface receptors to nucleate CI assemblies, extracellular conditions that prolong the adaptation time of CI disproportionately enhance the aggregate NF-κB response. These observations are recapitulated in a model of NF-κB signaling by invoking mechanisms for DNA-binding and chromatin reorganization. The resulting system reveals how IKK-encoding of dynamic environmental conditions distinctly coordinate a range of potential NF-κB responses through systems feedback and chromatin remodeling.

542 **Methods**

543 **Cell Culture**

544 CRISPR-modified U2OS cells expressing N-terminal fusions of EGFP-NEMO and mCherry-
545 RelA from their endogenous loci[17], as well as KYM-1 cells stably expressing mVen-RelA, were
546 cultured in McCoy's 5A and RPMI medium respectfully at 37°C in a humidified incubator with
547 5% CO_2. The medium was supplemented with 10% fetal bovine serum (FBS) (Corning),
548 penicillin (100 U/mL), streptomycin (100 U/mL), and 0.2 mM L-glutamine (Invitrogen). Cells
549 were routinely screened for mycoplasma contamination.

550

551 **Live-cell imaging for pulse experiments in the microfluidic dynamical stimulation**
552 **system**

553 A custom microfluidic system, as previously described[24], was used for single and repeat
554 pulse experiments. Briefly, two-inlet PDMS devices were fabricated from corresponding 3D-
555 printed molds, sterilized by autoclaving, washed with ethanol, followed by PBS and
556 subsequently incubated with a 0.002% (v/v) fibronectin solution in PBS for 24 hours at 37°C.
557 U2OS double-CRISPR cells (~5×10^6 cells/mL) were seeded into the microfluidic devices
558 and incubated for at least 24 hours.

559

560 On the day of the experiment, the microfluidic device was connected using Tygon tubing to
561 fluid reservoirs on the gravity pump containing the appropriate treatments. FluoroBrite
562 DMEM medium (Gibco, A18967-01) supplemented with 10% FBS (Corning), penicillin (100
563 U/mL), streptomycin (100 U/mL), and 0.2 mM L-glutamine was used during imaging. IL-1 and

564 TNF treatments were prepared with Alexa Fluor 647–conjugated BSA (0.0025% v/v of a 5
565 mg/mL stock; Invitrogen) to visualize the cytokine containing stream in the device.
566
567 Images of EGFP-NEMO were acquired every 4 minutes using FITC filters, with a z-stack of
568 eight images at 0.5-μm intervals, using 0.04-second exposure and 32% transmission.
569 Similarly, mCherry-RelA was imaged every 4 minutes using the Alexa A594 filters, with 0.1-
570 second exposure and 50% transmission. Alexa Fluor 647–conjugated BSA was imaged every
571 1 minute using the CY5 channel with 0.1-second exposure and 50% transmission. All images
572 were acquired in an environmentally controlled chamber (37°C, 5% CO_2) on a DeltaVision
573 Elite microscope equipped with a pco.edge sCMOS camera and an Insight solid-state
574 illumination module (GE Healthcare) at 60x LUCPLFLN oil objective.
575
576 **Treating cells with 5-azacitidine**
577 U2OS double-tagged cells were treated with 5 uM of azacitidine (Sigma Aldrich, A2385) while
578 growing in a 10 cm dish. Since azacitidine is reported to degrade rapidly in aqueous solutions
579 at room temperature, cells received fresh 5 uM azacitidine daily for 3 or 6 days before
580 imaging. The day before imaging, cells were seeded on a 96-well plate at 6,000 cells/well.
581 On the day of imaging, the media in the wells were replaced with FluoroBrite DMEM
582 supplemented with FBS, penicillin, streptomycin, and L-glutamine. A single 6-minute pulse
583 of IL-1 at 50 ng/mL was given to the cells. 50 ng/mL was chosen because it most resembled
584 the IKK profile of a single 6-minute pulse of IL-1 in a microfluidic chip. Cells were imaged to
585 measure the nuclear localization of mCherry-RelA for 3 hours, with 4 minutes intervals.

586

587 **Extracting EGFP-NEMO and mCherry-RelA time profiles from live-cell images**

588 As previously decribed[63,64], dNEMO software was used to detect and quantify EGFP-NEMO
589 spots. The spot detection threshold in dNEMO was set between 2.1 and 2.4, and only spots
590 present in at least two contiguous slices of the 3D images were considered valid. Individual
591 cells were manually segmented using dNEMO's keyframing function. The mCherry-RelA
592 nuclear intensity trajectories were quantified using custom python scripts. Briefly, the
593 custom scripts allowed to identify regions of background and the nucleus across all frames
594 by defining regions by a box. Nuclear NF-kB was determined by calculating the mean pixel
595 intensity of the nucleus by the mean background intensity of the frame. Each cell trajectory
596 was manually tracked across all images. To calculate the fold change, mCherry-RelA
597 trajectories were divided by the initial nuclear fluorescence at time zero. The area under the
598 fold-change curve was calculated by first subtracting by 1 and setting any negative values
599 equal to 0. The trapezoidal function in MATLAB was used to calculate the area under the
600 curve from the data.

601 $$NFkBFC\ AUC = trapz(\max(NFkBFC - 1,0))$$

602 Where NFKBFC represents the fold change nuclear NF-kB.

603

604 **Mechanistic modeling**

605 The mechanistic model of NF-kB activation through IKK, called D2FC, was used as
606 previously published[32]. Briefly, the mechanistic model contains the key events from IKK
607 activation, degradation of IkB due to IKK, NF-kB translocation to the nucleus, and the up-

608 regulation of IkB in the cell. To interface the single-cell measurements of IKK punctate
609 formation, the D2FC model was modified such that the activation of IKK from its neutral state
610 depended on the formation of IKK punctate structures. The rate of formation is:

611 $$IKK_n \rightarrow IKK$$

612 $$Rate = k_a * IKKSpots(t) * IKK_n$$

613 The parameter k_a was optimized to reduce the sum of the squared error of the training data
614 and represents the parametrization of D2FC.

615

616 The input, IKKSpots(t), consists of experimental trajectories obtained from live-cell imaging.
617 These trajectories were fitted to a sum of four Gaussians using MATLAB's fit function. To
618 ensure that the fitted curve started at zero, additional weight was placed on the initial value
619 during optimization. Finally, all simulated IKK trajectories were visually inspected to confirm
620 that they captured the basic trends observed in the experimental data.

621 $$IKK(t) = \sum_{i=1}^{4} a_i e^{\left[-\left(\frac{(x-b_i)}{c_i}\right)^2\right]}$$

622 The parameters for each single cell IKK trajectory and mean IKK trajectory can be found in
623 the ModeledIKKTrajectories.xlsx supplementary information.

624

625 The D2FC[2] model introduced an additional mechanism that was necessary to fit the
626 emergent property as described in the results. The new mechanisms involved NF-κB binding
627 and opening new DNA-binding sites in chromatin. This mechanism includes a new model
628 species, NFκBDNA, representing NF-κB bound to DNA. The binding rate of NF-κB to DNA is

influenced by cooperative effects, where the presence of already-bound NF-κB increases the likelihood of additional NF-κB binding. This phenomenon reflects a so-called pioneering effect[49] in which the binding of NF-κB facilitates chromatin relaxation, opening more binding sites and enhancing NF-κB recruitment where Ps_0 represents the basal nuclear openness and was fixed to a value of 1:

$$NFkB \rightarrow NFkBDNA$$

$$Rate = ka1d * DCoop * NPio$$

$$DCoop = \frac{\left(\frac{NFkB}{\mathrm{kdNFKB}}\right)^{h2}}{1 + \left(\frac{NFkB}{\mathrm{kdNFKB}}\right)^{h2}}$$

$$NPio = Ps_0 + Ps * \frac{\left(\frac{NFkBDNA}{KDNA}\right)^{h3}}{1 + \left(\frac{NFkBDNA}{KDNA}\right)^{h3}}$$

NF-κB can dissociate from DNA either through direct binding of nuclear IκBα or via a basal rate of dissociation. The two methods follow basic mass action kinetics

$$IkBa + NFkBDNA \rightarrow IkBaNFkB$$

$$Rate = ka2a * [N.IkBa] * [N.NFkBDNA]$$

$$NFkBDNA \rightarrow NFkB$$

$$Rate = kd1d * [NFkBDNA]$$

Emergent property score

The emergent property score was calculated by first simulating nuclear RelA trajectories for each of the single cell trajectories of the single 6, single 15, and four 1.5-minute pulses. Since Fig. 2 showed an increase in the median AUC of nuclear RelA (fold change) between the single 6-minute and 4x1.5-minute pulses and between the single 6-minute pulse and single 15-minute pulse, the emergent property score was defined as follows:

$$Emergent\ Property\ Score = abs\left(\frac{med(AUC_{4x1.5})}{med(AUC_{1x6})} - \frac{med(\widehat{AUC_{4x1.5}}(\theta))}{med(\widehat{AUC_{1x16}}(\theta))}\right) + abs\left(\frac{med(AUC_{1x15})}{med(AUC_{1x6})} - \frac{med(\widehat{AUC_{1x15}}(\theta))}{med(\widehat{AUC_{1x16}}(\theta))}\right)$$

Where $\widehat{\mathrm{AUC}_{1\mathrm{x}6}}(\theta)$, $\widehat{\mathrm{AUC}_{1\mathrm{x}15}}(\theta)$, $\widehat{\mathrm{AUC}_{4\mathrm{x}1.5}}(\theta)$ represents the data set of single-cell predictions for the parameter set θ for the AUC of the nuclear RelA (fold change) for the 1x6, 1x15, and 4x1.5-minute pulses. AUC_{1x6}, AUC_{1x15}, and $AUC_{4x1.5}$ represent the area under the curve for the experimental single cell trajectories.

Model simulations

D2FC and D2FC^2 were built using MATLAB 2023a. Associated code is available through the supplement (Supplementary Files 2) and the following repository (https://github.com/recleelab/D2FCSquared/) . SimBiology was used to generate ordinary differential equations from the reaction rates. Models were simulated for 10 days without cytokine stimulation to ensure a steady state was reached. Then the IKK profile corresponding to the appropriate dose was simulated to get the simulated results. Particle swarm optimization from MATLAB's Global optimization toolbox was used to optimize the parameter set to fit the average results from four scenarios used for fitting which included

the control, 1x6 minute pulse, 1x30-minute pulse, and 4x1.5-minute pulse of IL-1. The global optimization attempted to minimize the following equation where $y_{i,t}$ is the experimental measurement for scenario i at time = t, and $\hat{y}_{i,t}(\theta)$ is the model estimate for parameter set θ:

$$J(\theta) = \sum_{i}\sum_{t}\left(y_{i,t} - \hat{y}_{i,t}(\theta)\right)^2 + NFkB_{Herusitic}(\theta)$$

Where:

$$NFkB_{Herusitic}(\theta) = \begin{cases} 0 & if\ 0.01 < R_{\frac{nuc}{cyt}} < 0.3 \\ 100 & if\ R_{\frac{nuc}{cyt}} < 0.01 \\ 5 * R_{\frac{nuc}{cyt}} & if\ R_{\frac{nuc}{cyt}} > 0.3 \end{cases}$$

The $NFkB_{Herusitic}$ was designed to ensure proposed parameters had a basal nuclear NF-kB described as the ratio of NF-kB in the nucleus to cytoplasm ($R_{\frac{nuc}{cyt}}$) within experimental expectations. Model values going below the lower limit were strongly penalized whereas models above were penalized proportional to ratio. The heuristic was set up to significantly penalize the overall optimization score if the basal nuclear NF-kB conditions were not met.

Particle swarm optimization was run with a swarm size of 100 particles and ceased after 20 consecutive iterations to prevent stalling, where the system could not achieve a reduction in the optimization score. Parameter values were optimized in $\log_{10}$ format to help the optimizer explore the full parameter space across multiple orders of magnitude. The prior distribution of parameters ranges for optimization were carefully selected to represent biophysically relevant ranges around each parameter in the D2FC model (Supplementary table 4).

690

691 **Quantification of zero- vs. first-order nuclear export kinetics**

692 Single-cell trajectories of nuclear NF-kB fold change were classified as having first- or zero-
693 order nuclear export kinetics by fitting two models to data at the point of nuclear NF-kB
694 exiting the nucleus. A linear model was fit between the point of decay and the last data point.
695 The first order decay model was fitted by setting N_0 to the value of decay and finding the k
696 value that minimized the sum of squared error. To avoid parameters for the first order decay
697 rate that are linear, a minimum parameter exponential rate constant of k was set to 0.0167
698 min^{-1} which represents a first order decay rate where approximately 95% of the nuclear Rela
699 would exit the nucleus within 180 minutes. Defining a maximum value was essential to
700 create a single metric for differentiating first and zero order decay rates.

701

702 Zero-Order Decay Model:

703 $$y = m * t + b$$

704

705 First-Order Decay model:

706 $$y(t) = N_0 * e^{-k*t}$$

707

708 For each single-cell trajectory, the time point of nuclear NF-kB exit rate was identified and
709 the first and zero order models were fit to the data, only considering points after NF-kB
710 started to exit the nucleus. The sum of squared error (SSE) was determined for both models
711 and the nuclear RelA exit rate score is calculated to be the difference between the $SSE_{Zero} -$

712 SSE_{First}. Positive values indicate zero-order and negative values indicate first-order nuclear
713 export kinetics.
714
715 **Benchmarking the quality of the single cell predictions**
716 Single-cell IKK trajectories were used as input for the model to generate predictions for each
717 cell. The sum of squared errors (SSE) was calculated for each of the 194 single-cell model
718 predictions to assess their accuracy. To classify the quality of these predictions, we
719 established thresholds for 'excellent,' 'high,' and 'poor' fits. The threshold for 'high' fits was
720 determined using an elbow plot. This was done by gradually increasing the threshold and
721 counting the number of unacceptable fits (see Supplementary Fig. 7). To identify the elbow
722 point, we first drew a line connecting the first and last points on the plot. We then measured
723 the perpendicular distances from each point on the elbow plot to this line. The point with the
724 maximum distance from the line was selected as the elbow point, which defined the optimal
725 threshold for high-quality fits. To further classify the single cell trajectories, we divided the
726 single cell trajectories between simulations that were considered excellent (which was
727 defined as half of the elbow point) and high-quality fits.
728
729 **SimBiology model**
730 A mechanistic model was constructed using SimBiology (MATLAB) by employing command-
731 line tools within an m-file, rather than the graphical interface. This approach enhanced
732 flexibility and automation in model development and simulation. SimBiology was used as a

733 tool to automate the process of converting from reaction rate equations to a set of ordinary
734 differential equations (ODE).
735
736 **Simulated CI Trajectories**
737 Simulated CI trajectories were generated by first creating an zeros array with one value set
738 to 1, representing the peak time. The array had a length of 46, matching the number of
739 timepoints in our time-lapse imaging. The peak was positioned at 28 (index position 7)
740 minutes, and a linear interpolation filled in the values between timepoints 0–28 and 28 to a
741 variable adaptation time, resulting in trajectories with a triangular shape. To aid downstream
742 fitting to Gaussian equations, a rolling average with a window of 3 was applied to smooth the
743 trajectory. The smoothed CI trajectories were then fit to the sum of four Gaussian equations,
744 for simulation in the model. To ensure simulation started at zero, additional weight was
745 added to t=0 to the optimization function. With the method, we can precisely control the
746 peak height, peak time, and adaptation time for the CI trajectories.
747
748 **Simulation of Chromatin Opening**
749 Chromatin opening to simulate azacitidine treatment was done by increasing the basal
750 chromatin openness parameter, Ps_0. To estimate the effect of chromatin permissiveness on
751 the fraction of free NF-κB, a sub-model was constructed that included only the binding and
752 unbinding of NF-κB to DNA. In this model, only free and bound NF-κB were dynamic, while
753 all other species, specifically IκBα, were held constant at the steady state value before CI
754 formation. The rate of NF-κB binding to DNA was determined by the equation:

755 $$Rate_{Binding} = ka1d * DCoop * NPio_{const} * [N.NFkB]$$

756 where $NPio_{const}$ was held constant during the simulation but varied for generating the
757 heatmap in Fig. 7C (bottom-right). The rate of NF-κB unbinding from DNA was influenced by
758 both the basal dissociation rate and binding to IκBα. IκBα was set to a constant value, equal
759 to the steady state value after 10 days of simulation, to ensure the sub-model closely
760 resembled the full model. Parameters from the best-fitting D2FC2 model were used for the
761 simulations.

762 $$Rate_{unbinding} = kd1d * [N.NFkBDNA] + ka2a * [N.IkBa_{steady-state}] [N.NFkBDNA]$$

763
764

References

1 Hatton, I. A. *et al.* The human cell count and size distribution. *Proceedings of the National Academy of Sciences* **120**, e2303077120, doi:10.1073/pnas.2303077120 (2023).

2 Hoesel, B. & Schmid, J. A. The complexity of NF-κB signaling in inflammation and cancer. *Molecular Cancer* **12**, 86, doi:10.1186/1476-4598-12-86 (2013).

3 Taniguchi, K. & Karin, M. NF-κB, inflammation, immunity and cancer: coming of age. *Nature Reviews Immunology* **18**, 309-324, doi:10.1038/nri.2017.142 (2018).

4 Staudt, L. M. Oncogenic activation of NF-kappaB. *Cold Spring Harb Perspect Biol* **2**, a000109, doi:10.1101/cshperspect.a000109 (2010).

5 Raj, A. & van Oudenaarden, A. Nature, nurture, or chance: stochastic gene expression and its consequences. *Cell* **135**, 216-226, doi:10.1016/j.cell.2008.09.050 (2008).

6 Elowitz, M. B., Levine, A. J., Siggia, E. D. & Swain, P. S. Stochastic gene expression in a single cell. *Science* **297**, 1183-1186, doi:10.1126/science.1070919 (2002).

7 Wen, J. D. *et al.* Following translation by single ribosomes one codon at a time. *Nature* **452**, 598-603, doi:10.1038/nature06716 (2008).

8 Livingston, N. M. *et al.* Bursting translation on single mRNAs in live cells. *Mol Cell* **83**, 2276-2289 e2211, doi:10.1016/j.molcel.2023.05.019 (2023).

9 Son, M., Wang, A. G., Keisham, B. & Tay, S. Processing stimulus dynamics by the NF-κB network in single cells. *Experimental & Molecular Medicine* **55**, 2531-2540, doi:10.1038/s12276-023-01133-7 (2023).

10 Micheau, O. & Tschopp, J. Induction of TNF receptor I-mediated apoptosis via two sequential signaling complexes. *Cell* **114**, 181-190 (2003).

11 Barnhart, B. C. & Peter, M. E. The TNF receptor 1: a split personality complex. *Cell* **114**, 148-150, doi:10.1016/s0092-8674(03)00561-0 (2003).

12 Laplantine, E. *et al.* NEMO specifically recognizes K63-linked poly-ubiquitin chains through a new bipartite ubiquitin-binding domain. *EMBO J* **28**, 2885-2895, doi:10.1038/emboj.2009.241 (2009).

13 Clark, K., Nanda, S. & Cohen, P. Molecular control of the NEMO family of ubiquitin-binding proteins. *Nat Rev Mol Cell Biol* **14**, 673-685, doi:10.1038/nrm3644 (2013).

14 Haas, T. L. *et al.* Recruitment of the linear ubiquitin chain assembly complex stabilizes the TNF-R1 signaling complex and is required for TNF-mediated gene induction. *Mol Cell* **36**, 831-844, doi:10.1016/j.molcel.2009.10.013 (2009).

15 Kim, A. H., Chiknas, P. M. & Lee, R. E. C. Ubiquitin: Not just a one-way ticket to the proteasome, but a therapeutic dial to fine-tune the molecular landscape of disease. *Clin Transl Med* **14**, e1769, doi:10.1002/ctm2.1769 (2024).

16 Tarantino, N. *et al.* TNF and IL-1 exhibit distinct ubiquitin requirements for inducing NEMO-IKK supramolecular structures. *J Cell Biol* **204**, 231-245, doi:10.1083/jcb.201307172 (2014).

17 Cruz, J. A. *et al.* A variable-gain stochastic pooling motif mediates information transfer from receptor assemblies into NF-kappaB. *Sci Adv* **7**, doi:10.1126/sciadv.abi9410 (2021).

18 Chen, Z. J. Ubiquitination in signaling to and activation of IKK. *Immunol Rev* **246**, 95-106, doi:10.1111/j.1600-065X.2012.01108.x (2012).

19 Israel, A. The IKK complex, a central regulator of NF-kappaB activation. *Cold Spring Harb Perspect Biol* **2**, a000158, doi:10.1101/cshperspect.a000158 (2010).

20 Nelson, D. E. *et al.* Oscillations in NF-κB Signaling Control the Dynamics of Gene Expression. *Science* **306**, 704-708, doi:doi:10.1126/science.1099962 (2004).

21 Ashall, L. *et al.* Pulsatile Stimulation Determines Timing and Specificity of NF-κB-Dependent Transcription. *Science* **324**, 242-246, doi:10.1126/science.1164860 (2009).

22 Cheng, Q. J. *et al.* NF-κB dynamics determine the stimulus specificity of epigenomic reprogramming in macrophages. *Science* **372**, 1349-1353, doi:doi:10.1126/science.abc0269 (2021).

23 Lee, R. E., Qasaimeh, M. A., Xia, X., Juncker, D. & Gaudet, S. NF-kappaB signalling and cell fate decisions in response to a short pulse of tumour necrosis factor. *Sci Rep* **6**, 39519, doi:10.1038/srep39519 (2016).

24 Mokashi, C. S., Schipper, D. L., Qasaimeh, M. A. & Lee, R. E. C. A System for Analog Control of Cell Culture Dynamics to Reveal Capabilities of Signaling Networks. *iScience* **19**, 586-596, doi:10.1016/j.isci.2019.08.010 (2019).

25 Thiemicke, A., Jashnsaz, H., Li, G. & Neuert, G. Generating kinetic environments to study dynamic cellular processes in single cells. *Sci Rep* **9**, 10129, doi:10.1038/s41598-019-46438-8 (2019).

26 Dettinger, P. *et al.* Automated Microfluidic System for Dynamic Stimulation and Tracking of Single Cells. *Anal Chem* **90**, 10695-10700, doi:10.1021/acs.analchem.8b00312 (2018).

27 Lee, R. E. C., Qasaimeh, M. A., Xia, X., Juncker, D. & Gaudet, S. NF-κB signalling and cell fate decisions in response to a short pulse of tumour necrosis factor. *Scientific Reports* **6**, 39519, doi:10.1038/srep39519 (2016).

28 Thiemicke, A. & Neuert, G. Kinetics of osmotic stress regulate a cell fate switch of cell survival. *Sci Adv* **7**, doi:10.1126/sciadv.abe1122 (2021).

29 Son, M. *et al.* NF-kappaB responds to absolute differences in cytokine concentrations. *Sci Signal* **14**, doi:10.1126/scisignal.aaz4382 (2021).

30 Blum, Y. *et al.* Temporal perturbation of ERK dynamics reveals network architecture of FGF2/MAPK signaling. *Mol Syst Biol* **15**, e8947, doi:10.15252/msb.20198947 (2019).

31 Ryu, H. *et al.* Frequency modulation of ERK activation dynamics rewires cell fate. *Mol Syst Biol* **11**, 838, doi:10.15252/msb.20156458 (2015).

32 Lee, Robin E. C., Walker, Sarah R., Savery, K., Frank, David A. & Gaudet, S. Fold Change of Nuclear NF-κB Determines TNF-Induced Transcription in Single Cells. *Molecular Cell* **53**, 867-879, doi:https://doi.org/10.1016/j.molcel.2014.01.026 (2014).

33 Zhang, Q. *et al.* NF-κB Dynamics Discriminate between TNF Doses in Single Cells. *Cell systems* **5**, 638-645.e635, doi:10.1016/j.cels.2017.10.011 (2017).

850 34 Kellogg, R. A., Tian, C., Lipniacki, T., Quake, S. R. & Tay, S. Digital signaling decouples
851 activation probability and population heterogeneity. *Elife* **4**, e08931,
852 doi:10.7554/eLife.08931 (2015).
853 35 Hazuda, D. J., Lee, J. C. & Young, P. R. The kinetics of interleukin 1 secretion from
854 activated monocytes. Differences between interleukin 1 alpha and interleukin 1
855 beta. *J Biol Chem* **263**, 8473-8479 (1988).
856 36 Kudo, S., Mizuno, K., Hirai, Y. & Shimizu, T. Clearance and tissue distribution of
857 recombinant human interleukin 1 beta in rats. *Cancer Res* **50**, 5751-5755 (1990).
858 37 Chapman, P. B. *et al.* Clinical pharmacology of recombinant human tumor necrosis
859 factor in patients with advanced cancer. *J Clin Oncol* **5**, 1942-1951,
860 doi:10.1200/JCO.1987.5.12.1942 (1987).
861 38 Oyler-Yaniv, J. *et al.* Catch and Release of Cytokines Mediated by Tumor
862 Phosphatidylserine Converts Transient Exposure into Long-Lived Inflammation. *Mol*
863 *Cell* **66**, 635-647 e637, doi:10.1016/j.molcel.2017.05.011 (2017).
864 39 Hoffmann, A., Levchenko, A., Scott, M. L. & Baltimore, D. The IκB-NF-κB Signaling
865 Module: Temporal Control and Selective Gene Activation. *Science* **298**, 1241-1245,
866 doi:doi:10.1126/science.1071914 (2002).
867 40 Kennedy, J. & Eberhart, R. in *Proceedings of ICNN'95 - International Conference on*
868 *Neural Networks*. 1942-1948 vol.1944.
869 41 Natoli, G., Saccani, S., Bosisio, D. & Marazzi, I. Interactions of NF-kappaB with
870 chromatin: the art of being at the right place at the right time. *Nat Immunol* **6**, 439-
871 445, doi:10.1038/ni1196 (2005).
872 42 Martone, R. *et al.* Distribution of NF-kappaB-binding sites across human
873 chromosome 22. *Proc Natl Acad Sci U S A* **100**, 12247-12252,
874 doi:10.1073/pnas.2135255100 (2003).
875 43 Brignall, R., Moody, A. T., Mathew, S. & Gaudet, S. Considering Abundance, Affinity,
876 and Binding Site Availability in the NF-kappaB Target Selection Puzzle. *Front*
877 *Immunol* **10**, 609, doi:10.3389/fimmu.2019.00609 (2019).
878 44 Zhao, B. *et al.* The NF-kappaB genomic landscape in lymphoblastoid B cells. *Cell*
879 *Rep* **8**, 1595-1606, doi:10.1016/j.celrep.2014.07.037 (2014).
880 45 Link, V. M. *et al.* Analysis of Genetically Diverse Macrophages Reveals Local and
881 Domain-wide Mechanisms that Control Transcription Factor Binding and Function.
882 *Cell* **173**, 1796-1809 e1717, doi:10.1016/j.cell.2018.04.018 (2018).
883 46 Stormberg, T., Filliaux, S., Baughman, H. E. R., Komives, E. A. & Lyubchenko, Y. L.
884 Transcription factor NF-κB unravels nucleosomes. *Biochim Biophys Acta Gen Subj*
885 **1865**, 129934, doi:10.1016/j.bbagen.2021.129934 (2021).
886 47 Lone, I. N. *et al.* Binding of NF-kappaB to nucleosomes: effect of translational
887 positioning, nucleosome remodeling and linker histone H1. *PLoS Genet* **9**,
888 e1003830, doi:10.1371/journal.pgen.1003830 (2013).
889 48 Sen, S., Cheng, Z., Sheu, K. M., Chen, Y. H. & Hoffmann, A. Gene Regulatory
890 Strategies that Decode the Duration of NFkappaB Dynamics Contribute to LPS-
891 versus TNF-Specific Gene Expression. *Cell Syst* **10**, 169-182 e165,
892 doi:10.1016/j.cels.2019.12.004 (2020).

49 Hansen, J. L., Loell, K. J. & Cohen, B. A. A test of the pioneer factor hypothesis using ectopic liver gene activation. *Elife* **11**, doi:10.7554/eLife.73358 (2022).
50 Christman, J. K. 5-Azacytidine and 5-aza-2'-deoxycytidine as inhibitors of DNA methylation: mechanistic studies and their implications for cancer therapy. *Oncogene* **21**, 5483-5495, doi:10.1038/sj.onc.1205699 (2002).
51 Werner, S. L., Barken, D. & Hoffmann, A. Stimulus specificity of gene expression programs determined by temporal control of IKK activity. *Science* **309**, 1857-1861, doi:10.1126/science.1113319 (2005).
52 Bergqvist, S. *et al.* Kinetic enhancement of NF-kappaBxDNA dissociation by IkappaBalpha. *Proc Natl Acad Sci U S A* **106**, 19328-19333, doi:10.1073/pnas.0908797106 (2009).
53 Grell, M., Wajant, H., Zimmermann, G. & Scheurich, P. The type 1 receptor (CD120a) is the high-affinity receptor for soluble tumor necrosis factor. *Proc Natl Acad Sci U S A* **95**, 570-575, doi:10.1073/pnas.95.2.570 (1998).
54 Mizel, S. B., Kilian, P. L., Lewis, J. C., Paganelli, K. A. & Chizzonite, R. A. The interleukin 1 receptor. Dynamics of interleukin 1 binding and internalization in T cells and fibroblasts. *J Immunol* **138**, 2906-2912 (1987).
55 Watanabe, N. *et al.* Continuous internalization of tumor necrosis factor receptors in a human myosarcoma cell line. *J Biol Chem* **263**, 10262-10266 (1988).
56 Werner, S. L. *et al.* Encoding NF-kappaB temporal control in response to TNF: distinct roles for the negative regulators IkappaBalpha and A20. *Genes & development* **22**, 2093-2101, doi:10.1101/gad.1680708 (2008).
57 Siggers, T. *et al.* Principles of dimer-specific gene regulation revealed by a comprehensive characterization of NF-kappaB family DNA binding. *Nat Immunol* **13**, 95-102, doi:10.1038/ni.2151 (2011).
58 Weigelin, B. *et al.* Cytotoxic T cells are able to efficiently eliminate cancer cells by additive cytotoxicity. *Nat Commun* **12**, 5217, doi:10.1038/s41467-021-25282-3 (2021).
59 Weigelin, B. & Friedl, P. T cell-mediated additive cytotoxicity - death by multiple bullets. *Trends Cancer* **8**, 980-987, doi:10.1016/j.trecan.2022.07.007 (2022).
60 Tian, B., Nowak, D. E. & Brasier, A. R. A TNF-induced gene expression program under oscillatory NF-kappaB control. *BMC Genomics* **6**, 137, doi:10.1186/1471-2164-6-137 (2005).
61 Wolf, B. K. *et al.* Cooperation of chromatin remodeling SWI/SNF complex and pioneer factor AP-1 shapes 3D enhancer landscapes. *Nat Struct Mol Biol* **30**, 10-21, doi:10.1038/s41594-022-00880-x (2023).
62 Vierbuchen, T. *et al.* AP-1 Transcription Factors and the BAF Complex Mediate Signal-Dependent Enhancer Selection. *Mol Cell* **68**, 1067-1082 e1012, doi:10.1016/j.molcel.2017.11.026 (2017).
63 Guo, Y., Kowalczyk, G. J. & Lee, R. E. C. Label and quantify mRNA molecules in live cell experiments using SunRISER and dNEMO. *STAR Protoc* **3**, 101630, doi:10.1016/j.xpro.2022.101630 (2022).

64 Kowalczyk, G. J. *et al.* dNEMO: a tool for quantification of mRNA and punctate structures in time-lapse images of single cells. *Bioinformatics* **37**, 677-683, doi:10.1093/bioinformatics/btaa874 (2020).

Acknowledgements

We thank other members of the Lee lab and colleagues in the Department of Computational and Systems Biology for many helpful discussions. This work was supported by generous funding to R.E.C.L. from NIH grant R35-GM119462.

943 **Figure legends**

944 **Fig. 1: NEMO features determine same-cell NF-kB responses to a single cytokine pulse.**
945 **A.** Schematic of a two-inlet, one outlet microfluidic chip with fluid flow from left to right. Inlet
946 1 (I1) contains a mixture of cytokine, dye, and medium, while inlet 2 (I2) contains only media.
947 The fluorescent dye is used exclusively to establish the position of the cytokine-containing
948 stream. U2OS cells are cultured and imaged within the central cell culture channel. On
949 average, 22 cells were imaged for each condition. **B.** Image of the custom gravity pump. Inlet
950 reservoirs I1 and I2 are connected to the orange basins and the outlet connected to the gray
951 basin. The gravity pump dynamically adjusts the relative heights of the basins to control fluid
952 flow. When the I1 basin is positioned lower than I2, cells are exposed to media only (top) and
953 when I1 is higher, cells are exposed to cytokine (bottom). **C.** Time-lapse images of CRISPR-
954 modified U2OS cells lines containing fluorescent protein fusions from their endogenous loci
955 (left; see also Supplementary Movie 1). Quantification of upstream activated receptor
956 complex measured through the formation and tracking of single EGFP-NEMO puncta (top).
957 Quantification of downstream activation of the NF-κB (RelA) transcriptional system
958 calculated by the fold change of mCh-RelA fluorescence in the nucleus (bottom). **D.** Single
959 cell time-courses for EGFP-NEMO spot numbers and nuclear mCh-RelA nuclear fold change
960 in response to a single pulse of IL-1 at 10 ng/ml with varying pulse durations. Light-colored
961 trajectories represent individual cells, while bold trajectories represent the average
962 response. **E.** The area under the curve (AUC) for the number of IL-1 induced spots (left) and
963 the fold change of nuclear RelA (right) increases with pulse duration. **F.** Same-cell
964 correlations from dual-reporter cells show the aggregate AUC of activated receptor

965 complexes and downstream transcriptional activity display a monotonic relationship
966 (Spearman ρ = 0.85).
967
968 **Fig. 2: NF-kB responses to a dose-conserving cytokine pulse train are enhanced.**
969 **A.** Single cell time-courses for EGFP-NEMO spot numbers and nuclear mCh-RelA nuclear
970 fold change responses to multiple short pulses. Single 6- and 15-minute pulses are shown
971 as reference points, representing equivalent and greater than twice the total cytokine
972 exposure, respectively, compared to the multiple short pulses (yellow highlighted
973 conditions; see also Supplementary Movies 1 and 2). On average, 20 single cells were
974 imaged per condition. **B.** The area under the curve (AUC) analysis of NEMO spot numbers
975 (left) shows no significant difference between single and multiple pulse stimulation
976 patterns. For comparison, the single 6- and 15-minute pulses do show a significant
977 difference (left). By contrast, the AUC for nuclear RelA fold change indicates a significant
978 difference between single and multiple pulse stimulation patterns (right). Median and
979 interquartile ranges are shown. **$P<10^{-2}$, student's t-test. **C.** The aggregate AUC of activated
980 receptor complexes and downstream transcriptional activity is not monotonic when
981 responses to multiple short pulses are combined.
982
983 **Fig. 3: Temporal features of NEMO spot numbers correlate with NF-kB and zero-order**
984 **export kinetics following a cytokine pulse train.**
985 **A.** Schematic of a typical NEMO spot trajectory highlighting features for the 'time to
986 maximum' (t_{max}) and 'adaptation time' (t_{adapt}). **B.** Boxplots showing t_{max} for single-cell

trajectories under 6-minute single and multi-pulse stimulation. **C.** Boxplots showing t_{adapt} for single-cell trajectories under 6-minute single and multi-pulse stimulation. **D.** Schematic of a typical nuclear RelA fold change trajectory highlighting the max fold change and the area under the curve (AUC). Additionally, examples for zero-order and first-order kinetics are illustrated for nuclear RelA export. **E.** Same cell correlations for time-courses of nuclear RelA exit rates scores and the t_{max} of NEMO. **F.** Same cell correlations for time-courses of nuclear RelA exit rates scores and the t_{adapt} of NEMO (min)

Fig. 4: A model with DNA-binding and chromatin remodeling recapitulates emergent properties of average cellular responses to dynamic stimuli.

A. Schematic of the mechanistic model fitting strategy. As input, the model uses experimental averages of EGFP-NEMO time-courses from four conditions, chosen to tune the model to the emergent property. Simulated NF-kB responses are compared against experimental results and used as a cost function for particle swarm optimization (PSO). **B.** Results of PSO from 500 replicates for each model architecture. Each model parameterization is evaluated based on the sum of squared error (SSE) to the 4 training conditions (x-axis), to the SSE of averages from the 5 validation conditions not used for PSO (y-axis), and emergent property error score (colorbar). D2FC optimized models were limited to the quadrant highlighted in pink. The red star indicates the overall best $D2FC^2$ model.

Fig. 5: $D2FC^2$ accurately predicts NF-kB responses using single cell CI data as inputs

A. Simulated single-cell NF-kB predictions using the best-performing $D2FC^2$ model using

1009 single-cell EGFP-NEMO as model inputs. **B and C.** Boxplots comparing the simulated and
1010 experimental AUC of nuclear RelA for single-pulse (B) and multi-pulse (C) dosing schedules.
1011 Between experiments and D2FC^2 simulations, the model shows remarkable similarity where
1012 only one condition has a statistically distinct difference (marked with *; $p < 0.05$, student's
1013 t-test). **D.** Proportion of single-cell predictions classified as excellent, high, or low quality
1014 (see also, Supplementary Fig. 7) compared to experimental data across different dosing
1015 schemes for the best-performing model (left). Overall performance of the top 10 models in
1016 predicting single-cell trajectories aggregated across all experimental conditions (right). See
1017 also Supplementary Table 3.
1018
1019 **Fig. 6: D2FC^2 accurately predicts cytokine-induced NF-kB responses following**
1020 **exposure to hypomethylating azacytidine.**
1021 **A.** Simulated estimate of baseline nuclear RelA (relative to original) in response increasing
1022 basal chromatin opening. **B.** Simulated nuclear RelA (fold change) using the average EGFP-
1023 NEMO time course from a single 6-min pulse as an input. Different colors represent
1024 indicated amounts of basal chromatin opening. **C.** Experimental measurements of basal
1025 nuclear RelA of cells exposed to 5 uM of Azacytidine for 3 and 6 days, respectively. **D.** Single-
1026 cell trajectories of nuclear RelA fold change for cells exposed to a single 6-minute pulse of
1027 IL-1 following azacytidine exposure for 3 or 6 days (top and bottom, respectively). Bold lines
1028 represent the average trajectory, and the shaded region is +/- 1 standard deviation. On
1029 average 26 cells were imaged in each condition. See also Supplementary Fig. 8.
1030

1031 **Fig. 7: Features of NF-kB responses show different sensitivities to features of CI**

1032 **A.** Schematic illustrating how NEMO features encoded by temporal stimulation impacts
1033 binding site availability and the duration of NF-κB retention. **B.** Simulated IKK trajectories
1034 varying the peak of NEMO numbers (top, peak), adaptation time of NEMO numbers (middle,
1035 t_{adapt}) independently. Combined features are used to generate simulated time-courses that
1036 scan the encoding space of NEMO puncta (bottom). **C.** Heatmap of: simulated peak nuclear
1037 RelA (fold change) with varying peak NEMO and adaptation times (top-left); Nuclear RelA
1038 export scores for simulated responses, where positive values indicate increasingly zero-
1039 order scores and negative values indicating the strength of first-order scores (top-right);
1040 Relative chromatin permissiveness, where higher values represent more open chromatin
1041 (bottom-left); and, results from a sub-model used to simulate the steady-state fraction of
1042 free nuclear NF-kB changes with overall nuclear NF-kB and chromatin permissiveness
1043 (bottom-right).

1044

Figure 1

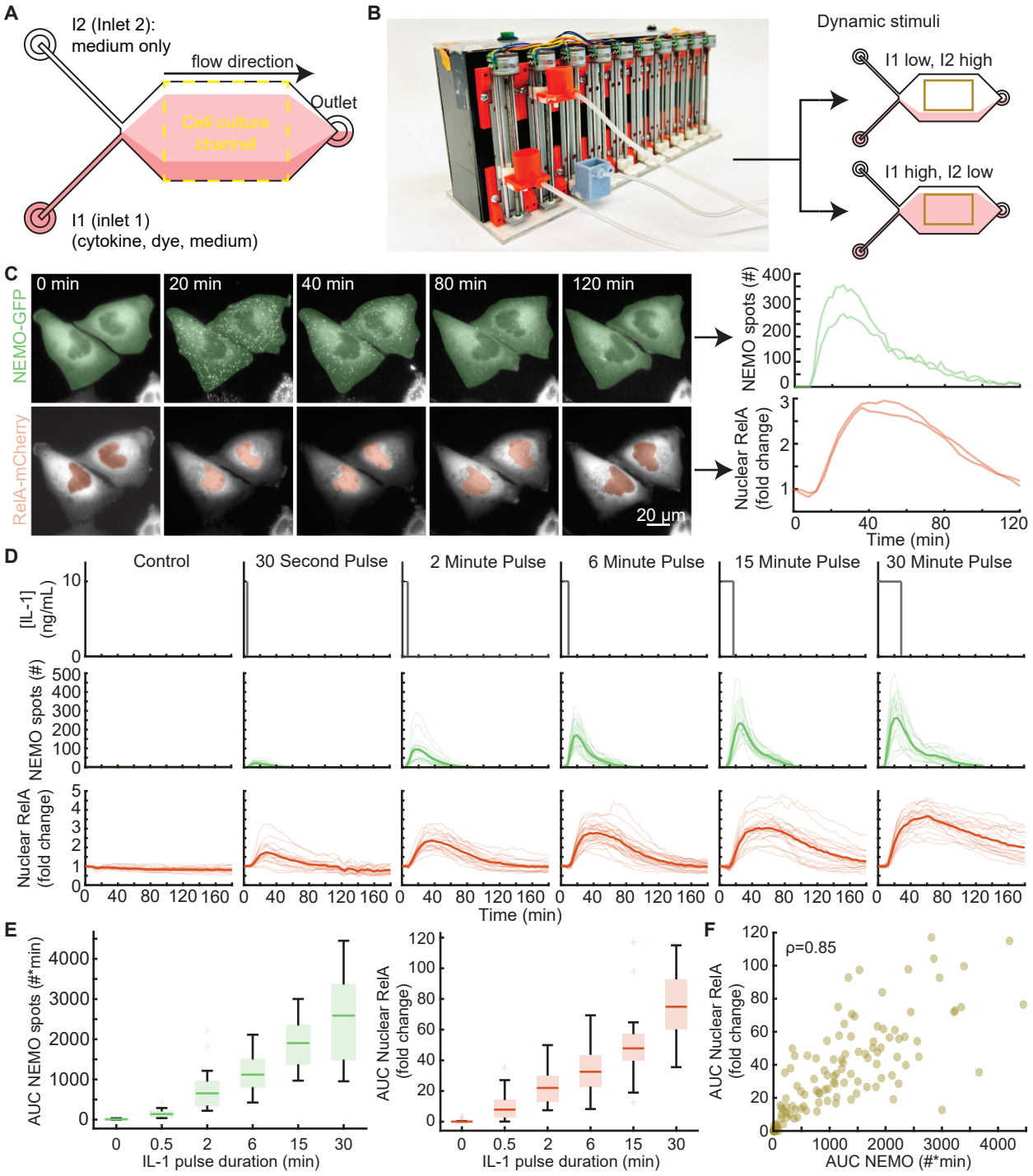
A
I2 (Inlet 2):
medium only
flow direction
Outlet
Cell culture
channel
I1 (inlet 1)
(cytokine, dye, medium)
B
Dynamic stimuli
I1 low, I2 high
I1 high, I2 low
C
NEMO-GFP
RelA-mCherry
0 min
20 min
40 min
80 min
120 min
20 μm
NEMO spots (#)
Nuclear RelA
(fold change)
Time (min)
D
Control
30 Second Pulse
2 Minute Pulse
6 Minute Pulse
15 Minute Pulse
30 Minute Pulse
[IL-1]
(ng/mL)
NEMO spots (#)
Nuclear RelA
(fold change)
Time (min)
E
AUC NEMO spots (#*min)
AUC Nuclear RelA
(fold change)
IL-1 pulse duration (min)
F
ρ=0.85
AUC Nuclear RelA
(fold change)
AUC NEMO (#*min)

Figure 2

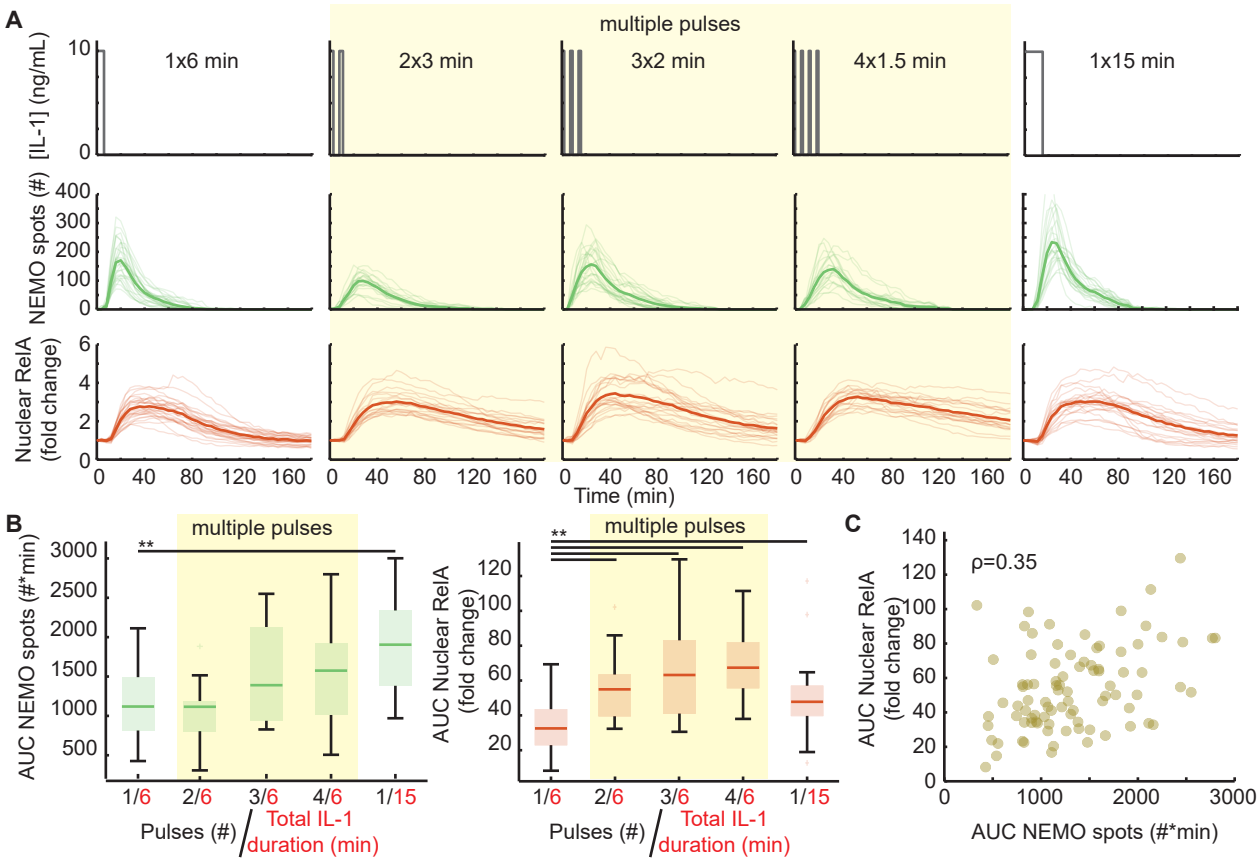
A
multiple pulses
1x6 min
2x3 min
3x2 min
4x1.5 min
1x15 min
[IL-1] (ng/mL)
NEMO spots (#)
Nuclear RelA (fold change)
Time (min)
B
AUC NEMO spots (#*min)
AUC Nuclear RelA (fold change)
**
1/6
2/6
3/6
4/6
1/15
Pulses (#) / Total IL-1 duration (min)
C
ρ=0.35
AUC Nuclear RelA (fold change)
AUC NEMO spots (#*min)

Figure 3

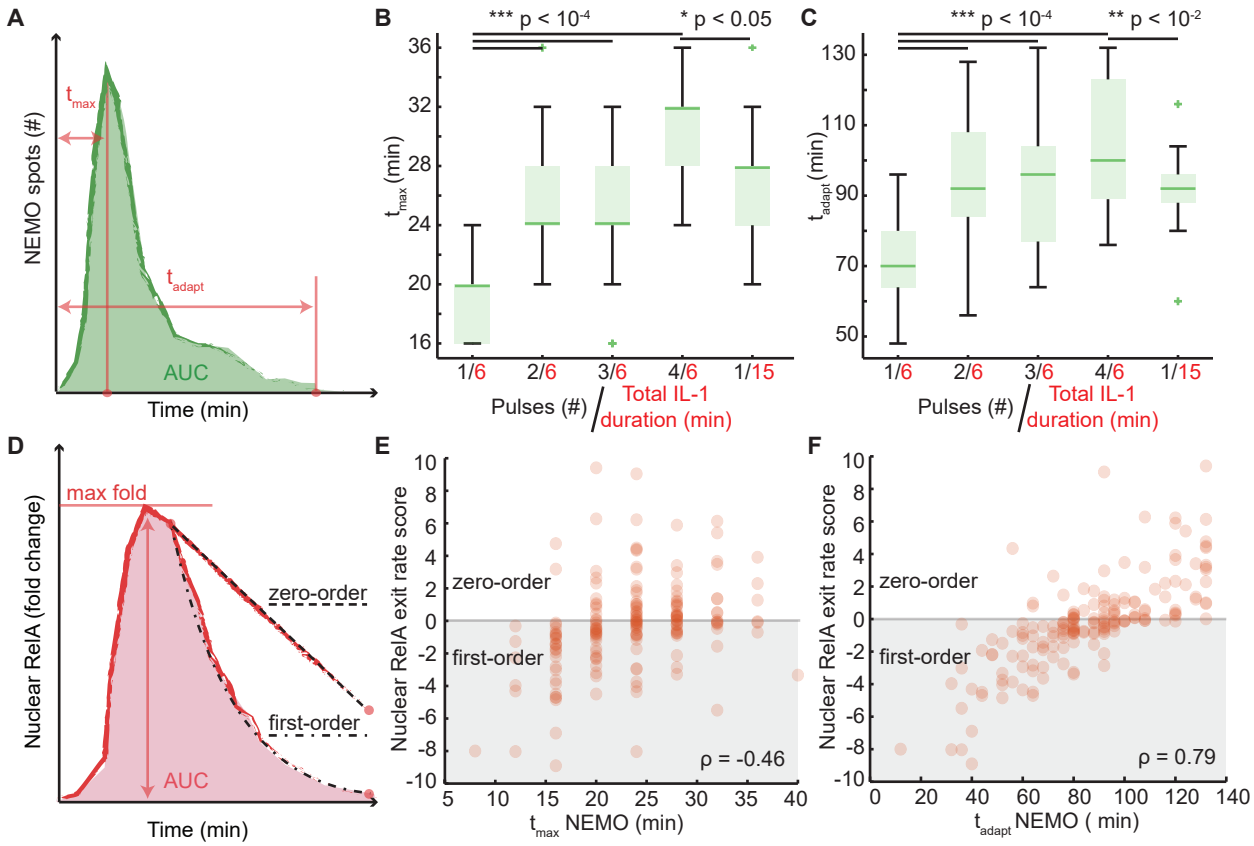
A
NEMO spots (#)
t_{max}
t_{adapt}
AUC
Time (min)
B
*** p < 10^{-4}
* p < 0.05
t_{max} (min)
1/6
2/6
3/6
4/6
1/15
Pulses (#) / Total IL-1 duration (min)
C
*** p < 10^{-4}
** p < 10^{-2}
t_{adapt} (min)
1/6
2/6
3/6
4/6
1/15
Pulses (#) / Total IL-1 duration (min)
D
Nuclear RelA (fold change)
max fold
zero-order
first-order
AUC
Time (min)
E
Nuclear RelA exit rate score
zero-order
first-order
ρ = -0.46
t_{max} NEMO (min)
F
Nuclear RelA exit rate score
zero-order
first-order
ρ = 0.79
t_{adapt} NEMO (min)

Figure 4

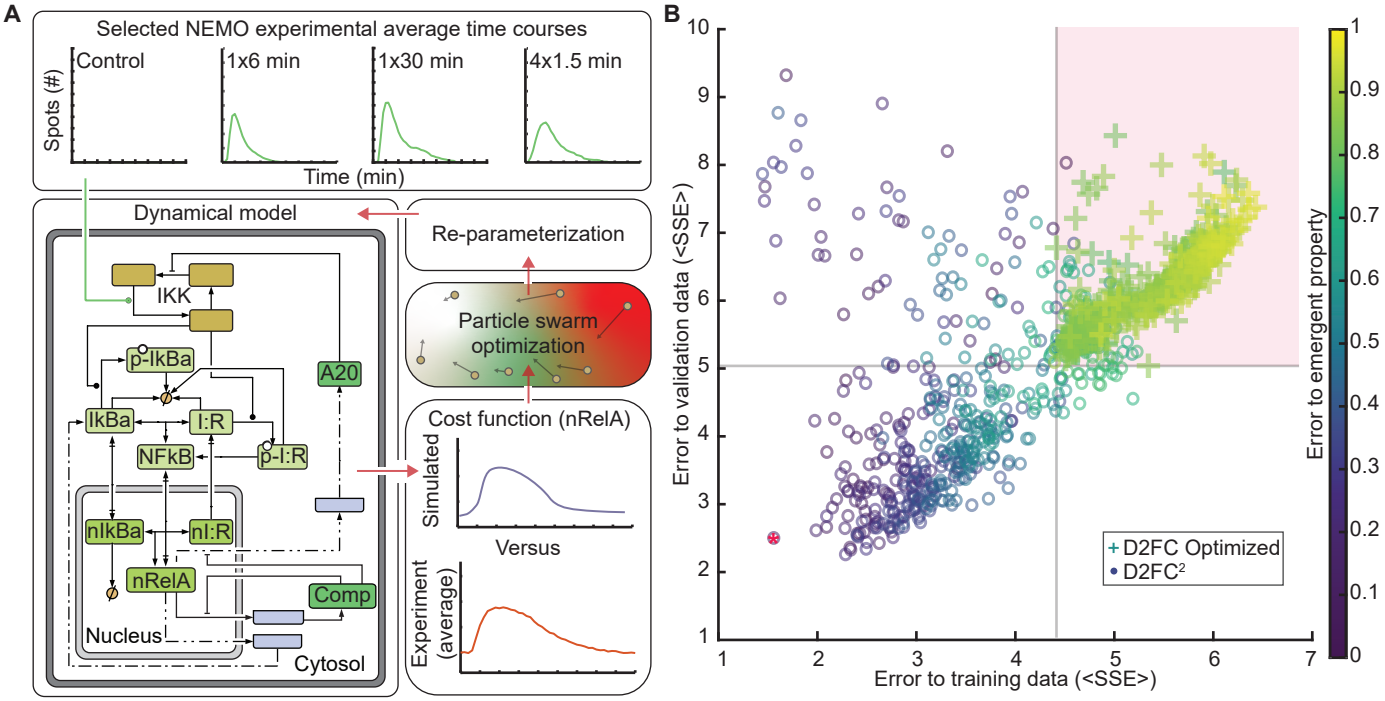
A
Selected NEMO experimental average time courses
Control
1x6 min
1x30 min
4x1.5 min
Spots (#)
Time (min)
Dynamical model
IKK
p-IkBa
A20
IkBa
I:R
NFkB
p-I:R
nIkBa
nI:R
nRelA
Comp
Nucleus
Cytosol
Re-parameterization
Particle swarm optimization
Cost function (nRelA)
Simulated
Versus
Experiment (average)
B
Error to validation data (<SSE>)
Error to training data (<SSE>)
Error to emergent property
D2FC Optimized
D2FC²

Figure 5

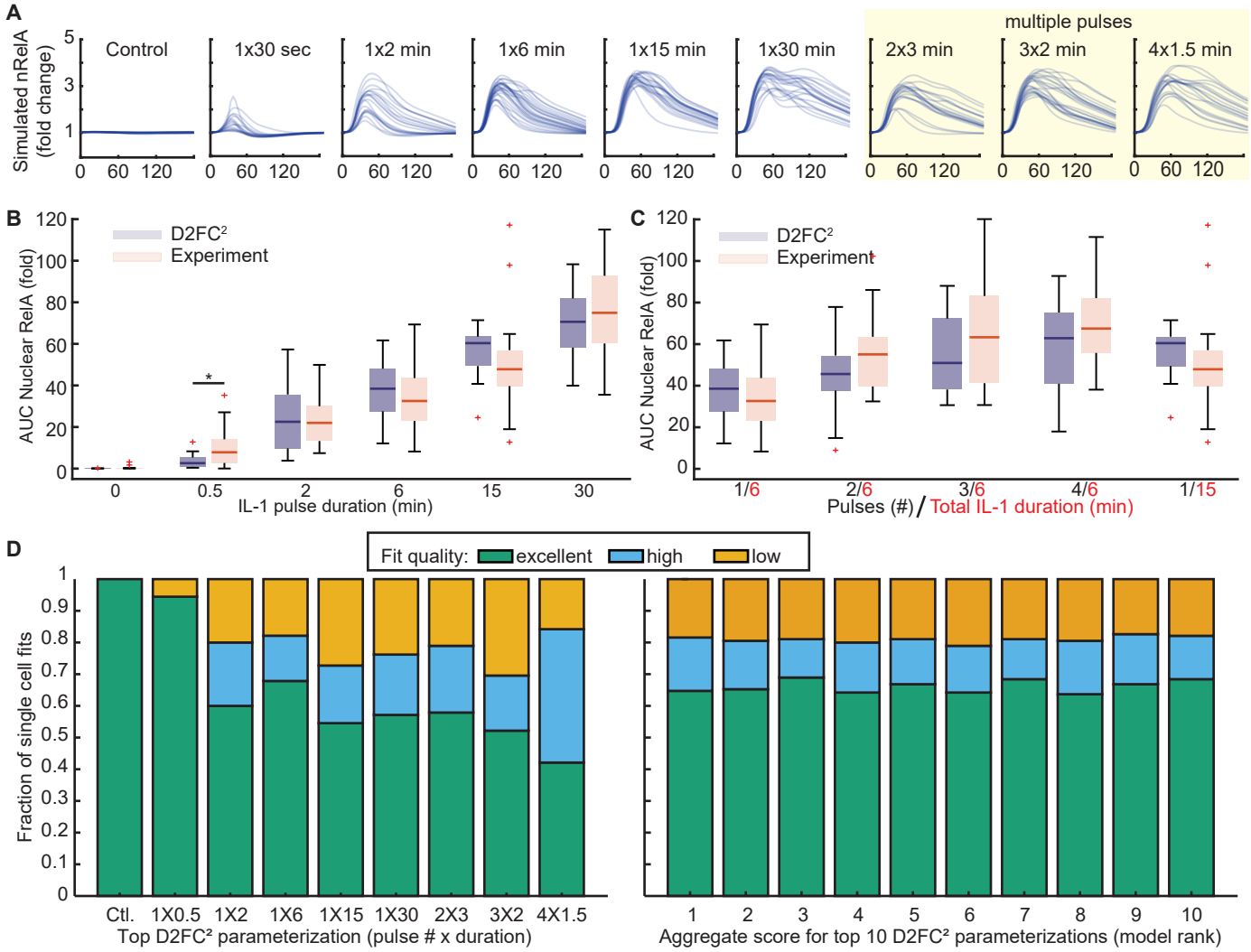
A
Simulated nRelA (fold change)
Control
1x30 sec
1x2 min
1x6 min
1x15 min
1x30 min
multiple pulses
2x3 min
3x2 min
4x1.5 min
B
AUC Nuclear RelA (fold)
D2FC²
Experiment
IL-1 pulse duration (min)
C
Pulses (#) / Total IL-1 duration (min)
D
Fit quality: excellent high low
Fraction of single cell fits
Ctl. 1X0.5 1X2 1X6 1X15 1X30 2X3 3X2 4X1.5
Top D2FC² parameterization (pulse # x duration)
Aggregate score for top 10 D2FC² parameterizations (model rank)

Figure 6

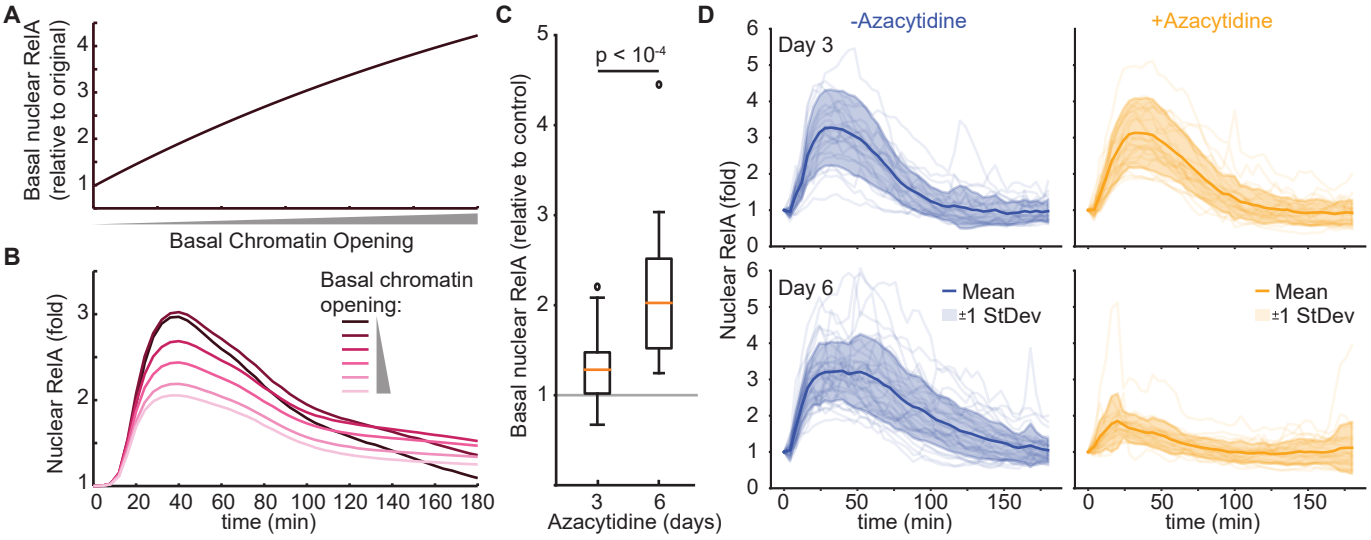
A
Basal nuclear RelA (relative to original)
Basal Chromatin Opening
B
Nuclear RelA (fold)
Basal chromatin opening:
time (min)
C
Basal nuclear RelA (relative to control)
p < 10-4
Azacytidine (days)
D
-Azacytidine
+Azacytidine
Day 3
Day 6
Mean
±1 StDev
Nuclear RelA (fold)
time (min)

Figure 7

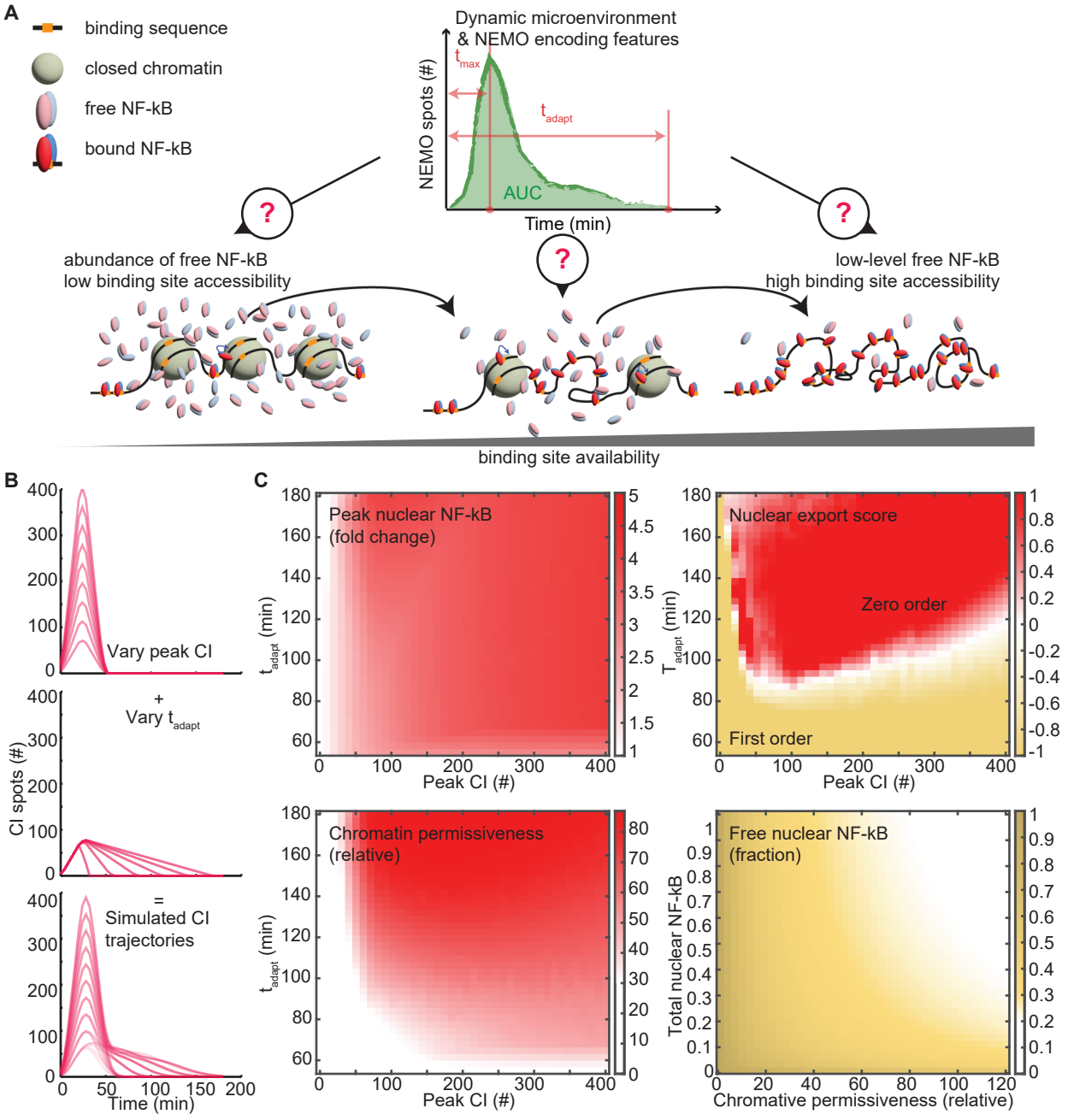
A
binding sequence
closed chromatin
free NF-kB
bound NF-kB
Dynamic microenvironment
& NEMO encoding features
NEMO spots (#)
t max
t adapt
AUC
Time (min)
?
abundance of free NF-kB
low binding site accessibility
low-level free NF-kB
high binding site accessibility
binding site availability
B
Vary peak CI
+
Vary t adapt
=
Simulated CI
trajectories
CI spots (#)
Time (min)
C
Peak nuclear NF-kB
(fold change)
Nuclear export score
Zero order
First order
Chromatin permissiveness
(relative)
Free nuclear NF-kB
(fraction)
t adapt (min)
T adapt (min)
Peak CI (#)
Total nuclear NF-kB
Chromative permissiveness (relative)

Supplementary Information

Time-varying stimuli that prolong IKK activation promote nuclear remodeling and mechanistic switching of NF-κB dynamics

Authors

Steven W. Smeal[1], Chaitanya S. Mokashi[1,2], A. Hyun Kim[1], P. Murdo Chiknas[1], Robin E. C. Lee[1,3,†]

Affiliations

[1]Department of Computational and Systems Biology, School of Medicine, University of Pittsburgh, Pittsburgh, PA 15213, USA

[2]current address Altos Labs, Redwood City, CA, 94065, USA

[3]Center for Systems Immunology, School of Medicine, University of Pittsburgh, Pittsburgh, PA 15213, USA

Other footnotes

[†] Corresponding Author: robinlee@pitt.edu

Supplementary files

Supplementary File 1: STL file for Y-channel microfluidic device. The included file can be 3D printed and used as a mold to produce the PDMS-based microfluidic device used in this study.

Supplementary File 2: D2FC^2 model files. The included model files are used for D2FC^2 and related simulations. See also the lab GitHub page for most up to date information (https://github.com/recleelab/D2FCSquared/)

Supplementary movies

Supplementary movie 1: Time-lapse images of CRISPR-modified U2OS cells. Fluorescent protein fusions at their endogenous loci are shown EGFP-NEMO (left) and mCherry-RelA (right). 60x images captured the response of two cells exposed to continuous to a saturating 1000 ng/mL of IL-1.

Supplementary movie 2: Time-lapse images of dual-reporter cells exposed to a single pulse. Dynamics of EGFP-NEMO (left) and mCherry-RelA (right) in response to a single 6-minute pulse of 10 ng/mL IL-1 in the microfluidic device. Cells display typical adaptive behavior within 100 minutes of stimulation.

Supplementary movie 3: Time-lapse images of dual-reporter cells exposed to four 1.5-minute pulses. Dynamics of EGFP-NEMO (left) and mCherry-RelA (right) in the microfluidic device exposed to 4x1.5-minute pulse of 10 ng/mL IL-1 with 5-minute gaps. Top cells displays prolonged EGFP-NEMO puncta and zero-order export kinetics, whereas the lower cell displays less-sustained EGFP-NEMO puncta and adapts within 180 minutes of stimulation.

Supplementary figures

Supplementary Figure 1: Dynamic stimulation device and cell responses to a single pulse

A. Schematic of the microfluidic chip as designed in the Autodesk Fusion 360 software highlighting the dimensions of the chip for the X, Y, and Z axis, units in mm. **B.** Image of the microfluidic chip with PDMS attached to a glass cover slide, coin for scale. Green food coloring was imaged to highlight the inlets, chamber, and outlets for image purposes only. **C.** Nuclear RelA export scores (see methods) for experimental trajectories of varying single pulse duration. **D.** Pairwise comparison of p-values for conditions in (C), student's t-test.

Figure S1

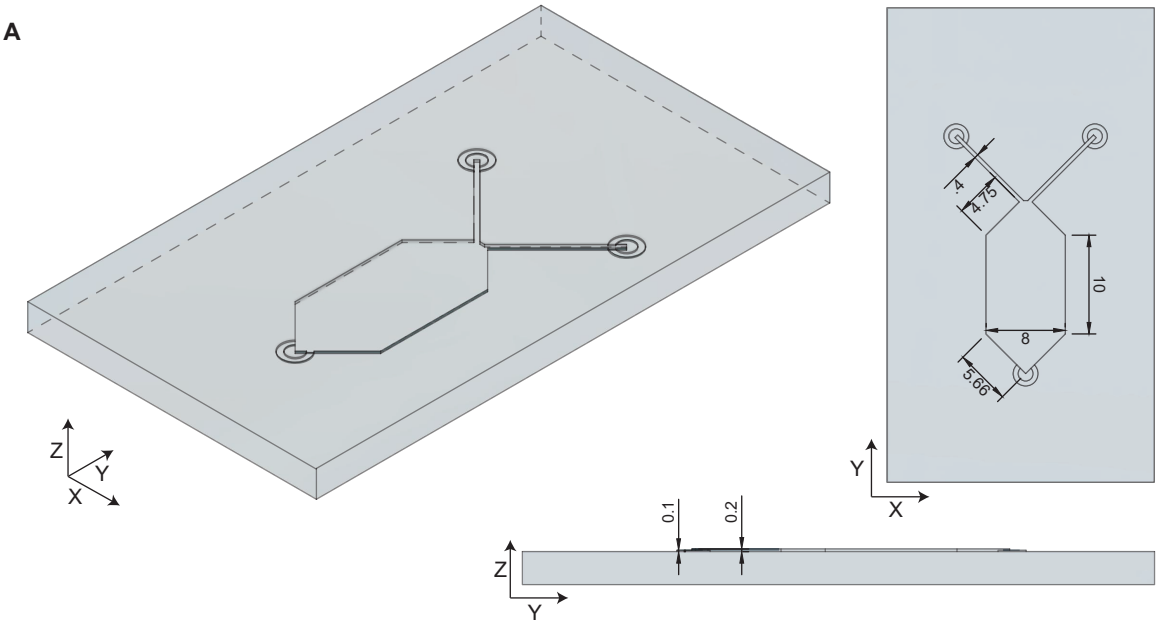

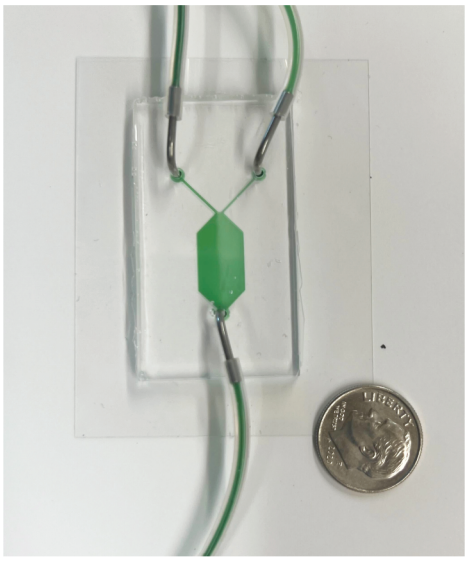

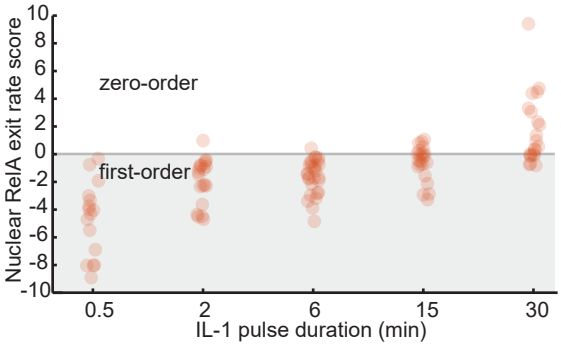

D

p-val	0.5 min	2 min	6 min	15 min	30 min
0.5 min	1	0.0002	3E-06	6E-07	1E-08
2 min	0.0002	1	0.4	0.004	3E-06
6 min	3E-06	0.4	1	0.007	3E-07
15 min	6E-07	0.004	0.007	1	0.0005
30 min	1E-08	3E-06	3E-07	0.0005	1

Supplementary Figure 2: NF-kB responses to a dose-conserving cytokine pulse train are enhanced for two and three pulse stimuli.

A. Boxplots of single-cell experimental time courses showing AUCs of NEMO spots (left) and Nuclear RelA (right). A 5-minute gap time between three 2-minute pulses of IL-1 at 10 ng/mL causes a significant enhancement of nuclear RelA. Increasing the gap time beyond 5-minutes has diminishing returns. **B.** Boxplots of single-cell experimental time courses as in panel A for two 3-minute pulses. Increasing the gap duration up to 15 minutes enhances the AUC of nuclear RelA. Boxplots show the median value and interquartile ranges. On average, 20 cells were imaged for each condition. P-values indicated for student's t-test.

Figure S2

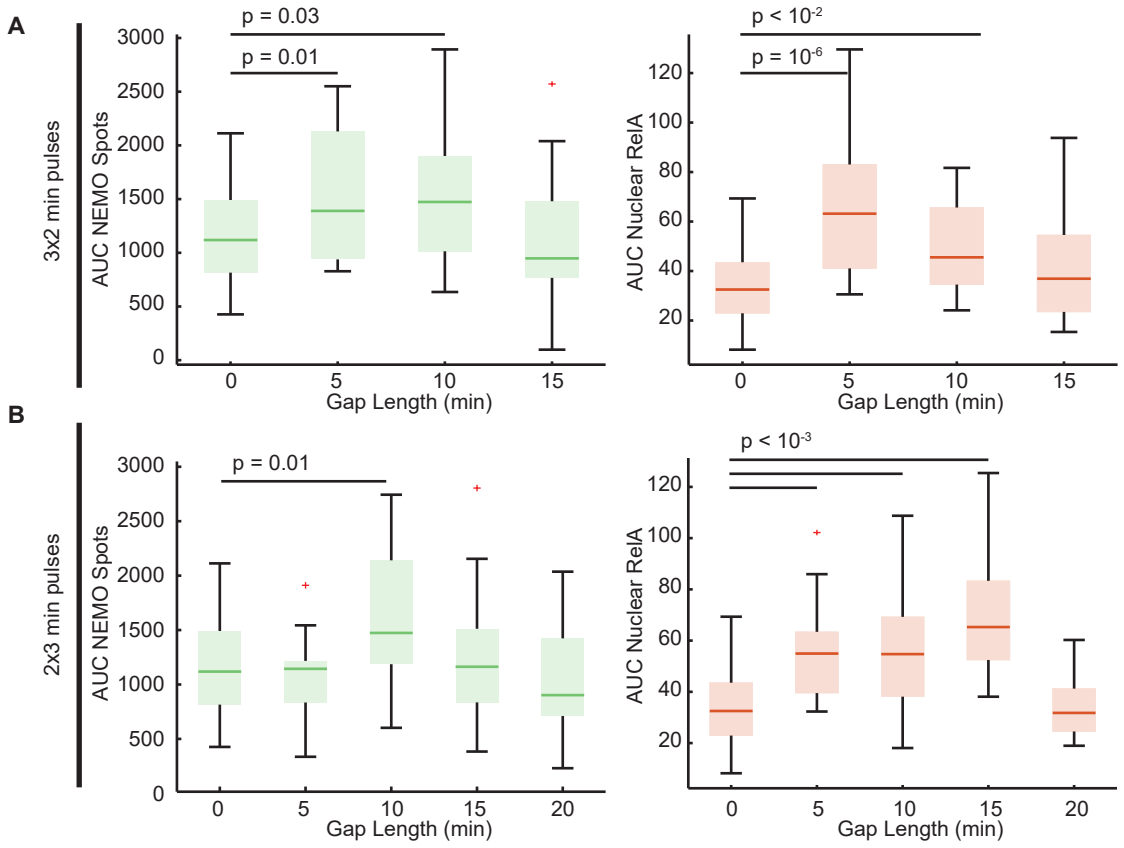
A
3x2 min pulses
AUC NEMO Spots
p = 0.03
p = 0.01
Gap Length (min)
AUC Nuclear RelA
p < 10-2
p = 10-6
Gap Length (min)
B
2x3 min pulses
AUC NEMO Spots
p = 0.01
Gap Length (min)
AUC Nuclear RelA
p < 10-3
Gap Length (min)

Supplementary Figure 3: KYM-1 cells exposed to a pulse train of TNF enhances the NF-kB response

A. Time lapse images of KYM-1 stably expressing mVen-RelA fusion exposed to TNF at 1 ng/mL as a single 6-minute pulse (top) or two 3-minute pulses with a 9-minute gap (bottom). **B.** Single cell trajectories of the intensity of nuclear RelA (fold change) for KYM-1 cells exposed to a continuous (left), single 6-minute (middle), and two 3-minute (right) pulses of TNF at 1 ng/mL. Orange bold lines represent mean and shaded region represents +/- 1 standard deviation of single cell trajectories. **C.** Box plots of the AUC of nuclear RelA (fold change) for varying the gap length of two 3-minute pulses (left) and two 2-minute pulses. Boxplots show the median value and interquartile ranges.

Figure S3

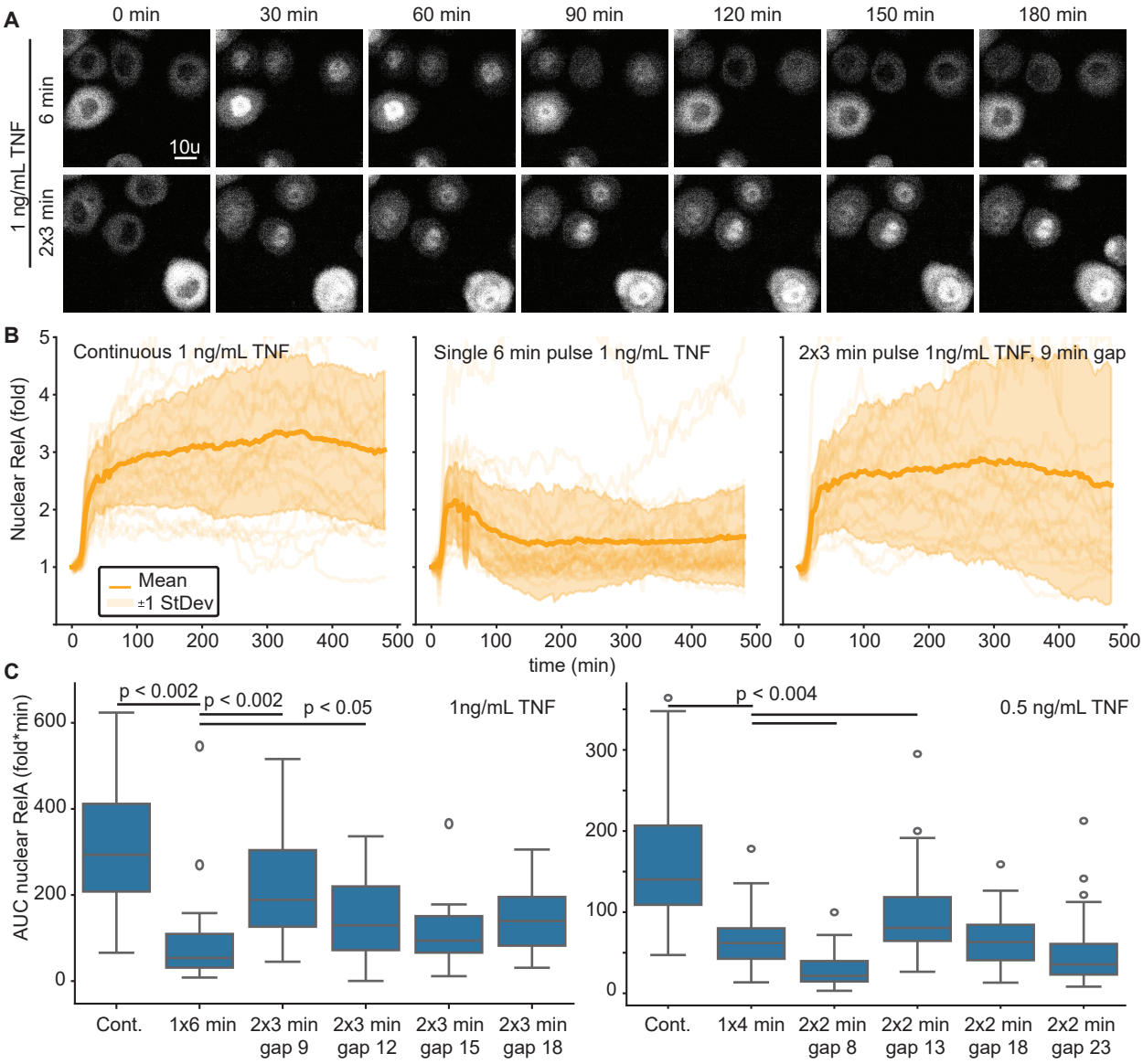
A
0 min
30 min
60 min
90 min
120 min
150 min
180 min
1 ng/mL TNF
6 min
2x3 min
10u
B
Continuous 1 ng/mL TNF
Single 6 min pulse 1 ng/mL TNF
2x3 min pulse 1ng/mL TNF, 9 min gap
Nuclear RelA (fold)
Mean
±1 StDev
time (min)
C
AUC nuclear RelA (fold*min)
p < 0.002
p < 0.002
p < 0.05
1ng/mL TNF
p < 0.004
0.5 ng/mL TNF
Cont.
1x6 min
2x3 min gap 9
2x3 min gap 12
2x3 min gap 15
2x3 min gap 18
1x4 min
2x2 min gap 8
2x2 min gap 13
2x2 min gap 18
2x2 min gap 23

Supplementary Figure 4: Dose-conserving pulse trains switch the export mechanism of nuclear RelA to a pseudo-zero-order process.

A. Box plot of the maximum nuclear RelA (fold change) of single cell trajectories given 10 ng/ml IL-1 for single and multiple short pulses. Although significant for 2 of the 5 conditions, the trend of increased nuclear RelA is only very subtle and does not explain the enhanced AUC in response to a cytokine pulse train. **B.** Example trajectories highlighting the exit rate score, used to distinguish first-order and zero-order export kinetics. Experimental data are representative single cell trajectories (solid red line) and dashed lines represent models of best fit for zero and first order decay. Positive scores represent zero-order export kinetics, and negative scores represent first-order kinetics. See methods for details. **C.** Jitter plot of exit rate scores for individual cell trajectories of the single- and multi-pulse IL-1 stimulation patterns (top). Pairwise comparisons indicate p-value for student's t-test (bottom).

Figure S4

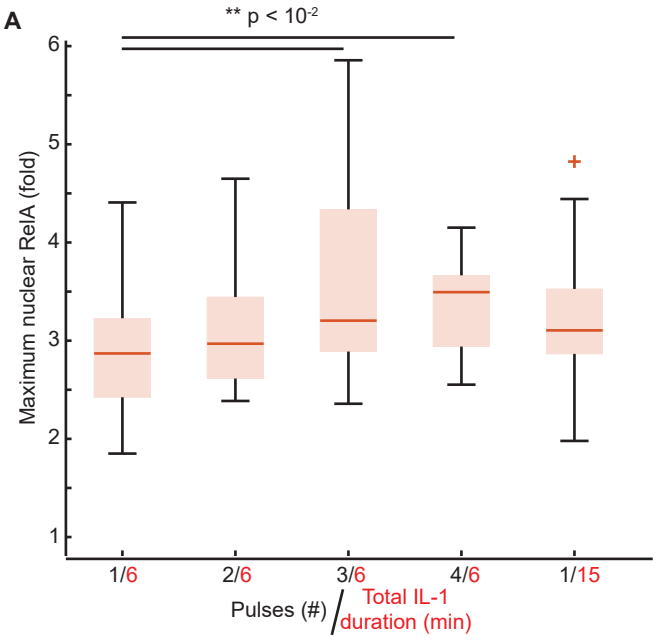

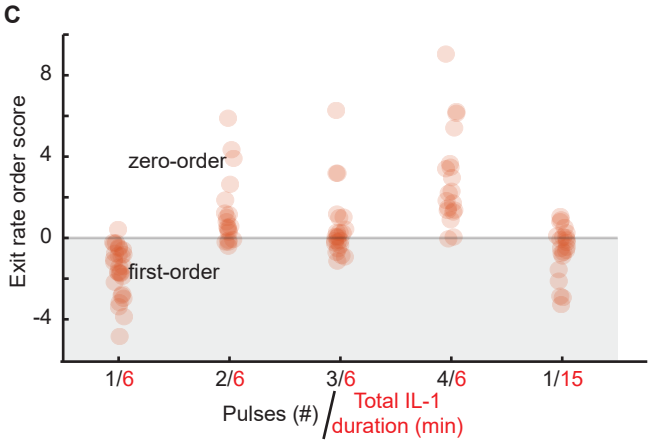

	1x6 min	2x3 min	3x2 min	4x1.5 min	1x15 min
1x6 min	1	4E - 08	3E-06	7E - 11	0.007
2x3 min	4E-08	1	0.1	0.02	0.0002
3x2 min	3E-06	0.1	1	0.0005	0.01
4x1.5 min	7E-11	0.02	0.0005	1	4E - 07
1x15 min	0.007	0.0002	0.01	4E - 07	1

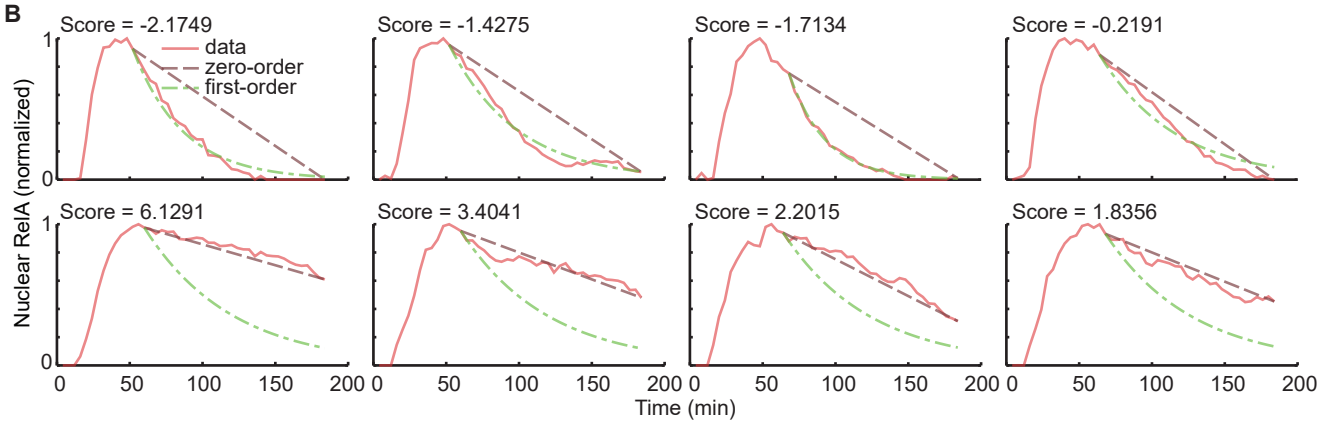

Supplementary Figure 5: Original D2FC and optimized parameterizations do not recapitulate the emergent property.

A and B. Box plots comparing the D2FC simulated results of the AUC nuclear RelA of the single (A) and multi-pulse (B) stimulation pattern. D2FC model is using original parameter set and D2FC optimized is the overall best set of parameters found from the particle swarm optimization. Statistically significant differences between models and experiment are indicated (*; $p<0.05$, student's t-test). The D2FC recapitulates responses to a single pulse, but not to pulse trains. Remarkably, the optimized D2FC fails to recapitulate most conditions. The relative failure of the optimized D2FC is because PSO using the emergent property (fits to averages from four selected conditions: control, 1x0.5-min, 4x1.5-min, 1x30-min) as an objective function effectively distributed the error across conditions, resulting in a model that marginally improves responses to a pulse train at the expense of even poorer fits to other conditions. **C.** Results of the D2FC, D2FC optimized, and $D2FC^2$ comparing simulated results (solid lines) with the averages of single-cell trajectories (circles) in each of three conditions. Simulation results for the D2FC optimized, and $D2FC^2$ are for lowest-error parameterizations following particle swarm optimization.

Figure S5

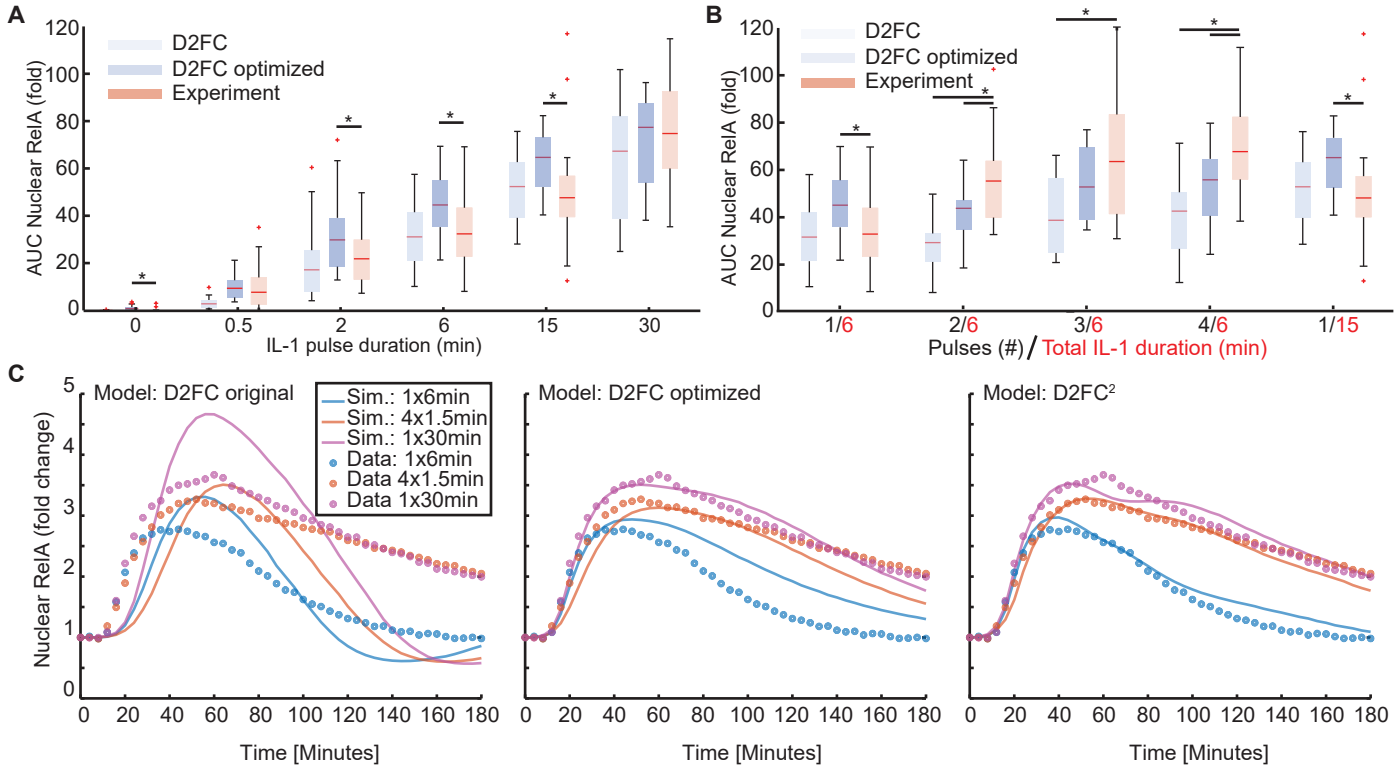
A
D2FC
D2FC optimized
Experiment
AUC Nuclear RelA (fold)
IL-1 pulse duration (min)
B
Pulses (#) / Total IL-1 duration (min)
C
Model: D2FC original
Model: D2FC optimized
Model: D2FC²
Sim.: 1x6min
Sim.: 4x1.5min
Sim.: 1x30min
Data: 1x6min
Data 4x1.5min
Data 1x30min
Nuclear RelA (fold change)
Time [Minutes]

Supplementary Figure 6: Post-hoc analysis of particle swarm optimization results for the D2FC^2.

A. Box plots of the parameters identified in 500 iterations of the D2FC^2 optimization using particle swarm. The y-axis is normalized relative to the parameter limits to account for differences in parameter orders. Importantly, for most parameters, there were solutions following particle swarm optimization that used the full range of values from the prior distribution suggesting that the parameter space has been effectively swarmed. **B.** Heat map of parameters for the top 10 models for the D2FC^2 normalized to the explored parameter space. Colorbar represents the normalized parameter value relative to the prior distribution (Supplementary Table 4). For most parameters there is variance between the models indicating that comparable results can be achieved via distinct parameter combinations.

Figure S6

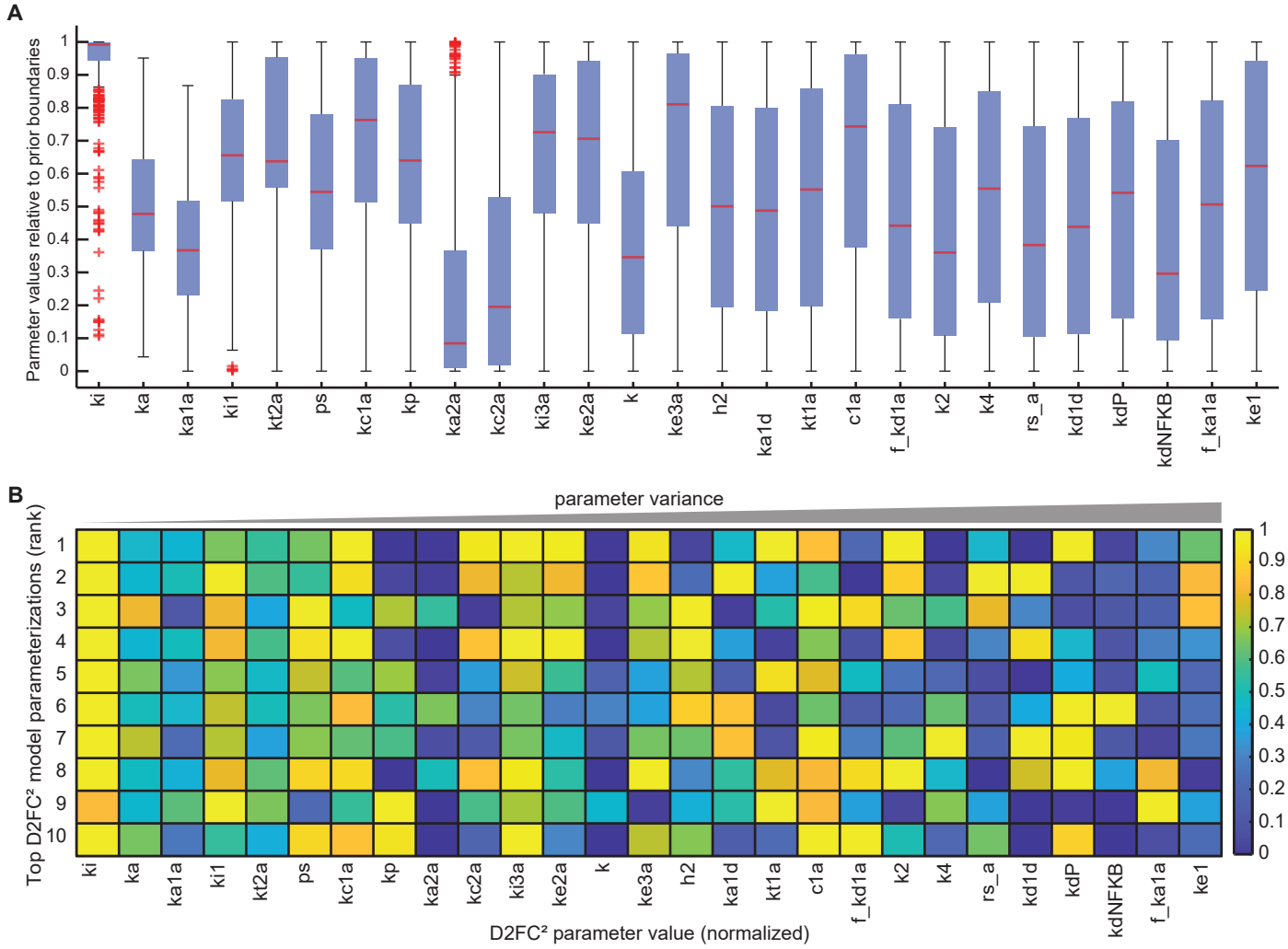
A
Parmeter values relative to prior boundaries
1
0.9
0.8
0.7
0.6
0.5
0.4
0.3
0.2
0.1
0
ki
ka
ka1a
ki1
kt2a
ps
kc1a
kp
ka2a
kc2a
ki3a
ke2a
k
ke3a
h2
ka1d
kt1a
c1a
f_kd1a
k2
k4
rs_a
kd1d
kdP
kdNFKB
f_ka1a
ke1
B
parameter variance
Top D2FC² model parameterizations (rank)
1
2
3
4
5
6
7
8
9
10
D2FC² parameter value (normalized)

Supplementary Figure 7: Quality of fit to single cell trajectories for the top D2FC^2 model parameterizations.

A. Elbow plot showing the fraction of non-acceptable fits as a function of the threshold for defining an acceptable single-cell trajectory. The elbow point, mathematically identified as the point furthest from a linear line connecting the first and last values (see Methods), was used to set a threshold between high- and poor-quality fits. A strict threshold of half the elbow point was applied to identify single cell simulations fits that are considered excellent.

B. Example simulated single cell trajectories highlighting the excellent, high, and poor single cell trajectories compared to the experimental data.

Figure S7

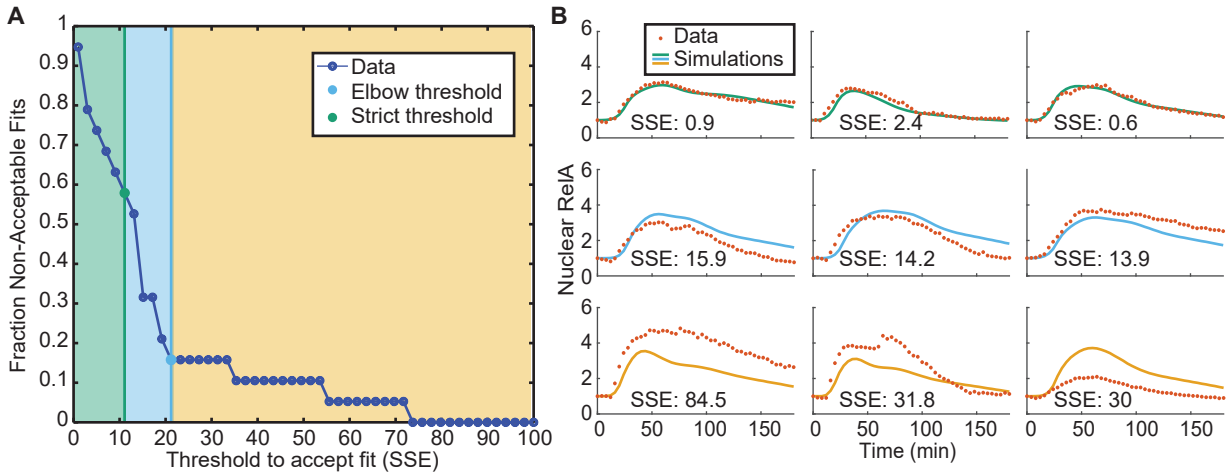
A
Fraction Non-Acceptable Fits
Threshold to accept fit (SSE)
Data
Elbow threshold
Strict threshold
B
Data
Simulations
Nuclear RelA
Time (min)
SSE: 0.9
SSE: 2.4
SSE: 0.6
SSE: 15.9
SSE: 14.2
SSE: 13.9
SSE: 84.5
SSE: 31.8
SSE: 30

Supplementary Figure 8: 5-Azacytidine stimulation significantly reduces features of NF-kB responses.

A. Box plots of the maximum nuclear RelA (fold change) for single cell trajectories exposed to 5-azacytidine for indicated duration before exposure to a single 6-minute pulse of 10 ng/ml IL-1. **B.** Box plots of the AUC for nuclear RelA (fold change) for single cell trajectories exposed to 5-azacytidine for indicated duration before exposure to a single 6-minute pulse of 10 ng/ml IL-1. P-values represent a student's t-test.

Figure S8

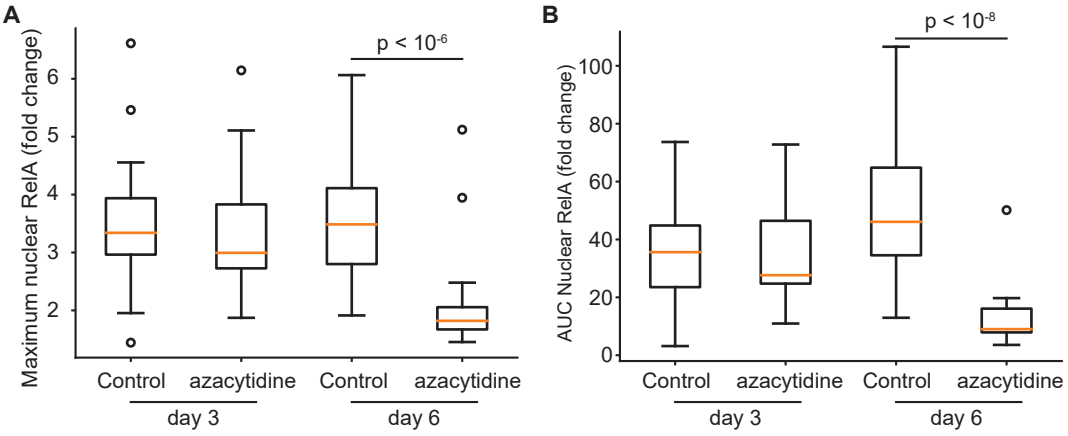
A
Maximum nuclear RelA (fold change)
6
5
4
3
2
p < 10-6
Control
azacytidine
Control
azacytidine
day 3
day 6
B
AUC Nuclear RelA (fold change)
100
80
60
40
20
0
p < 10-8
Control
azacytidine
Control
azacytidine
day 3
day 6

Supplementary tables

Supplementary Table 1: Summarizes reactions for the D2FC[2] model where "C." and "N." prefixes denote species is in the cytoplasm and nucleus, respectively. The column labeled "name" represents the parameter influencing the reaction rate. The reported values are from the best D2FC[2] model. The rows highlighted in gray represent added model mechanisms that differentiate between D2FC and D2FC[2]. Parameter kv (yellow; value = 3.3) accounts for subcellular compartment volumes between the cytoplasm and nucleus, applied to species traveling between the compartments. DCoop, NPio, NEnh1, NEnh2, and IKKSpots(t) are functions defined in supplementary table 2. Parameter ka (red) was used to optimize the original D2FC model to interface directly with NEMO spot numbers.

Reaction	Name	Value	Rate
$C.IkBa + C.NFkB \rightarrow C.IkBaNFkB$	ka1a	5.854E-01	$ka1a * [C.IkBa] * [C.NFkB]$
$C.IkBaNFkB \rightarrow C.IkBa + C.NFkB$	kd1a	5.000E-02	$kd1a * [C.IkBaNFkB]$
$C.NFkB \rightarrow N.NFkB$	ki1	5.403E-03	$kv * ki1 * [C.NFkB]$
$N.NFkB \rightarrow C.NFkB$	ke1	9.657E-05	$kv * ke1 * [N.NFkB]$
$N.NFkB + N.IkBa \rightarrow N.IkBaNFkB$	f_ka1a	4.25E-02	$f_ka1a * ka1a * [N.NFkB] * [N.IkBa]$
$N.IkBaNFkB \rightarrow N.NFkB + N.IkBa$	f_kd1a	2.625E-02	$f_kd1a * kd1a * [N.IkBaNFkB]$
$N.NFkB \rightarrow N.NFkBDNA$	ka1d	7.070E-04	$ka1d * DCoop * NPio * [N.NFkB]$
$N.NFkBDNA \rightarrow N.NFkB$	kd1d	6.684E-05	$kd1d * [N.NFkBDNA]$
$N.IkBa + N.NFkBDNA \rightarrow N.IkBaNFkB$	ka2a	1.320E-02	$ka2a * [N.IkBa] * [N.NFkBDNA]$
$N.IkBa \rightarrow \emptyset$	c4a	5.000E-04	$c4a * [N.IkBa]$
$C.IkBa \rightarrow \emptyset$	c4a	5.000E-04	$c4a * [C.IkBa]$
$N.IkBaNFkB \rightarrow C.IkBaNFkB$	ke2a	8.353E-02	$kv * ke2a * [N.IkBaNFkB]$
$C.IkBa \rightarrow N.IkBa$	ki3a	6.638E-03	$kv * ki3a * [C.IkBa]$
$N.IkBa \rightarrow C.IkBa$	ke3a	2.457E-03	$kv * ke3a * [N.IkBa]$
$C.IkBaNFkB \rightarrow C.NFkB$	c5a	2.200E-05	$c5a * [C.IkBaNFkB]$
$C.IKK \rightarrow C.IKKi$	ki	1.156E-02	$ki * [C.IKK]$
$C.IKKi \rightarrow C.IKKn$	kp	6.464E-05	$kp * [C.IKKi] * A20I$
$C.IKKn \rightarrow C.IKK$	ka	2.409E-06	$\mathrm{TR} * ka * \mathrm{IKKSpots(t)} * [C.IKKn]$
$\emptyset \rightarrow C.tIkBa$	rs_a	6.852E-08	$rs_a * (1 + NEnh1)$
$C.tIkBa \rightarrow \emptyset$	c3a	3.000E-04	$c3a * [C.tIkBa]$
$\emptyset \rightarrow C.IkBa$	c2a	5.000E-01	$c2a * C.tIkBa$
$\emptyset \rightarrow C.tCompetitor$	rs_a	6.852E-08	$rs_a * c1a * NEnh2$
$C.tCompetitor \rightarrow \emptyset$	c6a	4.290E-05	$c6a * [C.tCompetitor]$
$\emptyset \rightarrow C.Competitor$	c2a	5.000E-01	$c2a * [C.tCompetitor]$
$C.Competitor \rightarrow \emptyset$	c4a	5.000E-04	$c4a * [C.Competitor]$
$\emptyset \rightarrow C.tA20$	c1	2.000E-07	$c1 * NEen3$
$C.tA20 \rightarrow \emptyset$	c3	4.000E-04	$c3 * [C.Competitor]$
$\emptyset \rightarrow C.A20$	c2	5.000E-01	$c2 * [C.A20]$
$C.A20 \rightarrow \emptyset$	c4	4.500E-03	$c4 * [C.A20]$
$C.IkBa \rightarrow C.pIkBa$	kc1a	4.998E-01	$kc1a * [C.IKK] * [C.IkBa]$
$C.pIkBa \rightarrow \emptyset$	kt1a	5.796E-03	$kt1a * [C.pIkBa]$
$C.IkBaNFkB \rightarrow pIkBaNFkB$	kc2a	4.071E-01	$kc2a * [C.IKK] * [C.IkBaNFkB]$
$C.pIkBaNFkB \rightarrow C.NFkB$	kt2a	1.274E-04	$kt2a * [C.pIkBaNFkB]$

Supplementary Table 2: Algebraic equations used in the ordinary differential equations as shown in Supplementary Table 1 and used as outputs to the model.

Name	Equation	Notes
$DCoop$	$\frac{[N.NFkB]^{h2}}{(kdNFkB)^{h2} + [N.NFkB]^{h2}}$	Represents the cooperative effects of NFkB binding to DNA.
$NPio$	$1 + ps * \frac{[N.NFkBDNA]^{h3}}{(kdP)^{h3} + [N.NFkBDNA]^{h3}}$	Represents pioneering effect of NFKB can have on increasing the availed sites
$A20I$	$\frac{kbA20}{kbA20 + C.A20}$	Decrease rate of inactivated IKK converting to neutral IKK.
IKKSpots(t)	$IKK(t) = \sum_{i=1}^{4} a_i e^{\left[-\left(\frac{(x-b_i)}{c_i}\right)^2\right]}$	Parameters a_i, b_i, and c_i are fit to an experimental IKK spot profile. See supplementary information for complete set of parameters.
$NEnh1$	$c1a * \frac{[N.NFkB]^{h}}{k^{h} + [N.NFkB]^{h}}$	Increased rate of IkB transcription due to NFkB retained in nucleus.
$NEnh2$	$c1a * \frac{\left(\frac{[N.NFkB]}{k}\right)^{h+1}}{1 + \left(\frac{[N.NFkB]}{k}\right)^{h+1} + \left(\frac{[Competitor]}{k4}\right)^{h+1}}$	Increased rate of Competitor transcription where the competitor itself can reduce its own rate of transcription.
$NEen3$	$c1 * \frac{\left(\frac{[N.NFkB]}{k}\right)^{h+1}}{1 + \left(\frac{[N.NFkB]}{k}\right)^{h+1} + \left(\frac{[Competitor]}{k2}\right)^{h+1}}$	Increased rate of A20 transcription deepened upon NFkB nuclear localization and the rate can be reduced by competitor formation.
$N.NFkB_{Total}$	$[N.NFkB] + [N.IkBaNFkB] + [N.NFkBDNA]$	Total amount of NFkB in the nucleus including all forms which include free, bound to IkBa and bound to DNA
NFkB (Fold Change)	$\frac{[N.NFkB_{Total}]}{N.NFkB_{Total}(t = 0)}$	NFKB fold change that is directly comparable to the single cell data.

Supplementary Table 3: Parameterizations of the top 10 D2FC^2 models found through particle swarm optimization.

	Top 10 D2FC^2 parameterizations									
Name	1	2	3	4	5	6	7	8	9	10
ka1a	5.854E-01	1.018E+00	2.608E-02	9.137E-01	2.505E-01	6.583E-01	8.256E-02	4.916E-01	2.804E+00	1.209E-01
kd1a	5.000E-02	5.000E-02	5.000E-02	5.000E-02	5.000E-02	5.000E-02	5.000E-02	5.000E-02	5.000E-02	5.000E-02
ki1	5.403E-03	2.576E-02	1.068E-02	1.123E-02	5.843E-03	7.873E-03	7.284E-03	1.025E-02	2.519E-02	3.303E-03
ke1	9.657E-05	2.356E-04	2.576E-04	2.524E-05	1.353E-05	1.599E-05	1.788E-05	5.427E-06	2.994E-05	1.522E-05
f_ka1a	4.250E-02	2.148E-02	2.071E-02	3.878E-02	9.525E-02	1.620E-02	1.156E-02	4.217E-01	9.999E-01	1.340E-02
f_kd1a	2.625E-02	1.000E-02	6.686E-01	1.396E-02	9.097E-02	1.793E-02	3.747E-02	6.843E-01	5.618E-02	9.981E-01
ka1d	7.070E-04	1.147E-02	6.930E-05	4.376E-04	1.353E-04	5.532E-03	5.327E-03	1.122E-03	1.013E-03	1.336E-04
ps	7.951E+03	2.368E+03	6.744E+05	3.681E+05	2.878E+04	9.531E+03	1.154E+04	2.670E+05	1.932E+01	2.816E+05
h3	1.000E+00	1.000E+00	1.000E+00	1.000E+00	1.000E+00	1.000E+00	1.000E+00	1.000E+00	1.000E+00	1.000E+00
kdP	3.162E+00	1.123E+00	1.079E+00	1.691E+00	1.599E+00	3.162E+00	2.968E+00	3.160E+00	1.011E+00	2.797E+00
h2	1.500E+00	2.000E+00	1.641E+00	1.955E+00	1.502E+00	1.685E+00	1.998E+00	1.867E+00	1.501E+00	1.500E+00
kdNFKB	1.034E+00	1.308E+00	3.161E+00	3.096E+00	2.304E+00	2.773E+00	2.087E+00	1.434E+00	1.639E+00	2.174E+00
ka2a	1.320E-02	6.274E-02	2.672E-02	2.208E-02	2.197E-02	9.218E+01	2.695E-02	3.337E-01	1.067E-02	1.011E-02
kd1d	6.684E-05	6.919E-05	1.137E-03	6.429E-05	7.110E-05	2.005E-03	8.860E-05	8.467E-04	6.420E-05	6.551E-05
c4a	5.000E-04	5.000E-04	5.000E-04	5.000E-04	5.000E-04	5.000E-04	5.000E-04	5.000E-04	5.000E-04	5.000E-04
ke2a	8.353E-02	4.194E-02	2.341E-02	9.911E-02	1.361E-02	3.751E-03	8.649E-03	1.177E-02	1.549E-02	4.211E-03
ki3a	6.638E-03	1.907E-03	1.839E-03	6.038E-03	2.181E-03	1.318E-03	1.358E-03	5.267E-03	1.750E-03	6.700E-03
ke3a	2.457E-03	1.758E-03	7.948E-04	9.293E-04	1.906E-04	1.948E-04	6.694E-04	3.307E-03	3.572E-05	9.766E-04
c5a	2.200E-05	2.200E-05	2.200E-05	2.200E-05	2.200E-05	2.200E-05	2.200E-05	2.200E-05	2.200E-05	2.200E-05
ka	2.409E-06	2.263E-06	2.595E-05	2.120E-06	9.491E-06	3.078E-06	1.556E-05	2.706E-06	2.238E-06	9.295E-06
ki	1.156E-02	9.935E-03	1.130E-02	1.129E-02	1.138E-02	1.157E-02	1.160E-02	9.715E-03	4.903E-03	1.160E-02
kp	6.464E-05	7.738E-05	2.674E-03	9.060E-05	2.421E-03	1.016E-03	1.370E-03	6.441E-05	1.138E-02	8.211E-03
kbA20	1.800E-03	1.800E-03	1.800E-03	1.800E-03	1.800E-03	1.800E-03	1.800E-03	1.800E-03	1.800E-03	1.800E-03
c1a	1.525E+01	6.487E+00	2.227E+01	8.655E+00	1.245E+01	7.777E+00	2.158E+01	1.415E+01	1.421E+01	2.499E+01
h	2.000E+00	2.000E+00	2.000E+00	2.000E+00	2.000E+00	2.000E+00	2.000E+00	2.000E+00	2.000E+00	2.000E+00
k	6.681E-02	6.515E-02	7.179E-02	6.586E-02	1.263E-01	2.033E-01	9.796E-02	6.501E-02	3.657E-01	6.579E-02
rs_a	6.852E-08	9.820E-08	8.706E-08	6.178E-08	5.182E-08	5.435E-08	5.616E-08	5.001E-08	6.515E-08	7.825E-08
c3a	3.000E-04	3.000E-04	3.000E-04	3.000E-04	3.000E-04	3.000E-04	3.000E-04	3.000E-04	3.000E-04	3.000E-04
c2a	5.000E-01	5.000E-01	5.000E-01	5.000E-01	5.000E-01	5.000E-01	5.000E-01	5.000E-01	5.000E-01	5.000E-01
k4	1.018E-02	1.155E-02	1.479E-01	1.228E-02	2.641E-02	1.842E-01	9.652E-01	8.229E-02	2.209E-01	2.563E-02
c6a	4.290E-05	4.290E-05	4.290E-05	4.290E-05	4.290E-05	4.290E-05	4.290E-05	4.290E-05	4.290E-05	4.290E-05
c1	2.000E-07	2.000E-07	2.000E-07	2.000E-07	2.000E-07	2.000E-07	2.000E-07	2.000E-07	2.000E-07	2.000E-07
k2	9.979E-01	5.847E-01	1.847E-01	5.772E-01	3.202E-02	2.653E-02	1.675E-01	9.754E-01	1.171E-02	1.050E-01
c3	4.000E-04	4.000E-04	4.000E-04	4.000E-04	4.000E-04	4.000E-04	4.000E-04	4.000E-04	4.000E-04	4.000E-04
c2	5.000E-01	5.000E-01	5.000E-01	5.000E-01	5.000E-01	5.000E-01	5.000E-01	5.000E-01	5.000E-01	5.000E-01
c4	4.500E-03	4.500E-03	4.500E-03	4.500E-03	4.500E-03	4.500E-03	4.500E-03	4.500E-03	4.500E-03	4.500E-03
kc1a	4.998E-01	3.603E-01	6.169E-02	4.990E-01	1.010E-01	2.603E-01	1.095E-01	3.514E-01	8.498E-02	2.791E-01
kt1a	5.796E-03	2.681E-05	9.794E-05	1.160E-06	3.056E-03	1.410E-06	2.146E-06	9.194E-04	5.631E-03	6.875E-06
kc2a	4.071E-01	2.305E-01	9.433E-03	2.774E-01	3.883E-02	3.025E-02	1.465E-02	2.703E-01	9.620E-02	1.971E-02
kt2a	1.274E-04	1.760E-04	3.179E-05	1.616E-04	5.877E-05	7.688E-05	2.662E-05	2.133E-04	3.127E-04	3.724E-05

Supplementary Table 4: Prior boundaries of parameters used for particle swarm optimization of the D2FC and D2FC^2 models. D2FC values of N/A represent parameters that

were introduced in the D2FC[2] model. High and low parameter bounds are equal for parameter values that were held constant during optimization.

			Particle Swarm Parameter Bounds	
Name	D2FC Value	Units	Low	High
ka1a	0.5	1/(uM*sec)	1.00E-02	1.00E+02
kd1a	0.05	1/sec	0.05	0.05
ki1	0.0026	1/sec	0.00026	0.026
ke1	5.20E-05	1/sec	5.20E-06	5.20E-04
f_ka1a	N/A	dimensionless	0.01	1
f_kd1a	N/A	dimensionless	0.01	1
ka1d	N/A	1/sec	6.42E-05	1.16E-02
ps	N/A	dimensionless	1	1.00E+06
h3	N/A	dimensionless	1	1
kdP	N/A	uM/sec	1	3.1623
h2	N/A	dimensionless	1.5	2
kdNFKB	N/A	uM/sec	1	3.1623
ka2a	N/A	1/(uM *sec)	1.00E-02	1.00E+02
kd1d	N/A	1/sec	6.42E-05	1.16E-02
c4a	0.0005	1/sec	0.0005	0.0005
ke2a	0.01	1/sec	1.00E-03	1.00E-01
ki3a	0.00067	1/sec	6.70E-05	6.70E-03
ke3a	0.000335	1/sec	3.35E-05	3.35E-03
c5a	2.20E-05	1/sec	2.20E-05	2.20E-05
ka	2.00E-06	1/sec	1.00E-07	1.00E-04
ki	0.003	1/sec	6.42E-05	1.16E-02
kp	0.0006	1/sec	6.42E-05	1.16E-02
kbA20	0.0018	uM	0.0018	0.0018
c1a	1.00E+00	dimensionless	1.00E+00	2.50E+01
h	2	dimensionless	2.00E+00	2.00E+00
k	0.065	uM	6.50E-02	3.00E+00
rs_a	3.08E-06	uM/sec	5.00E-08	1.00E-07
c3a	0.0003	1/sec	0.0003	0.0003
c2a	0.5	1/sec	5.00E-01	5.00E-01
k4	0.065	uM	1.00E-02	1
c6a	4.29E-05	1/sec	4.29E-05	4.29E-05
c1	2.00E-07	uM /sec	2.00E-07	2.00E-07
k2	0.065	uM	1.00E-02	1
c3	0.0004	1/sec	0.0004	0.0004
c2	0.5	1/sec	0.5	0.5
c4	0.0045	1/sec	0.0045	0.0045
kc1a	0.074	1/(uM*sec)	0.009	0.5
kt1a	0.1	1/sec	1.00E-06	0.006
kc2a	0.37	1/(uM *sec)	0.009	0.5
kt2a	0.1	1/sec	1.00E-06	0.006